Gondwana Research 81 (2020) 312–338

Contents lists available at ScienceDirect

Gondwana Research

journal homepage: www.elsevier.com/locate/gr

Whole-rock geochemistry and U-Pb ages of Devonian bimodal-type rhyolites from the Rudny Altai, Russia: Petrogenesis and tectonic settings

M.L. Kuibida [a,b,*], O.V. Murzin [c], N.N. Kruk [a,b], I.Y. Safonova [a,b], M. Sun [d], T. Komiya [e], J. Wong [d], S. Aoki [e], N.M. Murzina [c], I. Nikolaeva [a], D.V. Semenova [a], M. Khlestov [a], R.A. Shelepaev [a,b], P.D. Kotler [a,b], V.A. Yakovlev [a,b], A.V. Naryzhnova [a]

[a] Sobolev Institute of Geology and Mineralogy SB RAS, Koptyuga ave. 3, Novosibirsk, Russia
[b] Novosibirsk State University, Pirogova st. 2, Novosibirsk, Russia
[c] Siberian Research Institute of Geology, Geophysics and Mineral Resources, Krasny prospect, 67, Novosibirsk, Russia
[d] Department of Earth Sciences, the University of Hong Kong, Pokfulam Road, Hong Kong, China
[e] University of Tokyo, 3-8-1 Komaba, Meguro-ku, Tokyo 153-8902, Japan

ARTICLE INFO

Article history:
Received 25 August 2019
Received in revised form 25 November 2019
Accepted 9 December 2019
Available online 27 December 2019

Handling Editor: S. Kwon

Keywords:
Rifted-arc
Back-arc basin
Bimodal basalt-rhyolite association
Melnichno-Sosnovsky volcanic complex
Central Asian Orogenic Belt

ABSTRACT

The paper presents new original data on the Devonian felsic volcanism of the NW Rudny Altai (Russia) in the west of Central Asian Orogenic Belt (CAOB) – the front part of the Altai convergent margin of the Siberian continent. Two geochemical types of subvolcanic rhyolites were emplaced synchronously with the bimodal rhyolite-basalt association, which began to form in the end-Emsian, and clearly manifested on the border of the Givetian and the Frasnian. The rhyolites yield zircon U-Pb ages of ca. 390 Ma (R1-type) and 380 Ma (R2- and R3-types), reflecting two peaks of the volcanic activity. Most of these rocks have extreme petrochemical characteristics of high SiO_2 contents and have contrast Na/K ratios. Their compositions are transition between calc-alkaline and tholeiite series: $(La/Yb)_n$ ~ 2–7, Zr/Y ~ 4 (Zr < 350 ppm) and La/Sm ~ 0.55–1. Rhyolites bear the distinctive geochemical signature of *A*-type felsic magma, such as enrichments in Zr, Nb, Y and Ce (>350 ppm), Zr (>250 ppm), and high Ga/Al (>2.6) values. The island-arc-like R1-rhyolite formed immediately after the beginning of rifting due to widespread crustal melting under reduced conditions. The generation of rift-like R2- and R3-rhyolites took place under non-equilibrium conditions, synchronously with the rise in the upper crust of Givetian-Frasnian basic magmas, as a result of the active lithospheric extension and high thermal input from the underlying hot mantle. We propose an extension regime in the transition area between the island-arc and back-arc basin for the origin of rhyolites. The study of the Devonian volcanism of the Rudny Altai gives important information about the processes that occurred at the initial stage of the formation of the Altai convergent margin.

1. Introduction

In the context of the analysis of magmatic formations, the early geosynclinal evolution of the marginal parts of the platforms is indicated by the formation of the so-called spilite-keratophyric association, which is a result of specific submarine explosive volcanism of essentially sialic-sodium composition (Daly, 1914; Rosenbursh, 1923; Battey, 1955; Kuznetsov, 1964). In case of rift-related extension of continental margins, mature island-arc, and marginal back-arc basin association is characterized by the predominance of felsic eruption and genetically related subvolcanic intrusions. Bimodal-felsic and bimodal-siliciclastic types are common (Barrie and Hannington, 1999), as manifested on the ancient Pacific margin of North America (New-Brunswick and Isok lake deposits in Canada), the modern Pacific margin of Asia (e.g. Hokuroku district of Japan), and the Paleo-Asian margin of Siberian continent (Rudny Altai; Lentz, 1998; Hart et al., 2004; Piercey et al., 2006; Galley et al., 2007; Gaboury and Pearson, 2008; Gaskov, 2015). In this paper, felsic volcanic rocks from the bimodal association of such geodynamic settings, are called “bimodal-type extensional rhyolites” (Bachmann and Bergantz, 2008; Tamura et al., 2009; Deering et al., 2008, 2010).

The Rudny Altai is located in the western part of the Central Asian Orogenic Belt (CAOB) or Altaid Tectonic Collage (Altaids) – the world's largest accretionary orogen, a Pacific-type system that comprises multiple subduction-accretionary orogens (e.g., Zonenshain et al., 1990; Mossakovsky et al., 1993; Sengör et al., 1993; Dobretsov et al., 1995; Jahn et al., 2000; Buslov et al., 2001; Yakubchuk, 2004; Buslov et al., 2004; Windley et al., 2007; Xiao et al., 2010; Safonova et al., 2011; Kröner et al., 2014; Xiao and Santosh, 2014; Chen et al., 2017; Safonova et al., 2018). The western Altaids segment extends for >2500 km from the Russian Ural in the west, across Eastern

* Corresponding author at: Sobolev Institute of Geology and Mineralogy SB RAS, Koptyuga ave. 3, Novosibirsk, Russia.
E-mail address: maxkub@igm.nsc.ru (M.L. Kuibida).

https://doi.org/10.1016/j.gr.2019.12.002
1342-937X/

Kazakhstan and Northwest China to Southern Mongolia. It developed in the Late Neoproterozoic-Late Paleozoic by closure and suturing of the Paleo-Asian Ocean (PAO), which once separated the Siberian Craton from the Tarim, North China and Kazakhstan continents. The PAO history continued for >800 Ma and included multiple events of subduction and accretion of oceanic island/plateau, island-arc, and terranes, of both western Pacific- and Andean-styles, which had eventually amalgamated into the Altaids in the Late Paleozoic.

The Altai orogenic belt (Bespaev et al., 1997; Scherba et al., 1998) or the Altai accretion-collision system (Vladimirov et al., 2003) is a Hercynian fold belt, extending for 2000 km from Russia and Kazakhstan through northern China to southwestern Mongolia (Sengör et al., 1993; Jahn et al., 2000; Buslov et al., 2001; Windley et al., 2007; Xiao et al., 2010; Pirajno, 2010; Cai et al., 2011). It developed along the Caledonian marginal terranes of the Siberian continent, due to the subduction and closure of Paleo-Asian Ocean, collision and post-collision tectonic processes. The formation of the Altai convergent margin is associated with the Devonian oblique subduction of the Chara oceanic plate under the terrain-orogenic margin of the Siberian continent. Tectonically, it consists of the frontal part (Rudny Altai), the axial (Central and Western Gorny Altai and Salair) and the rear part (Uimeno-Lebed in the Eastern Gorny Altai and Western Sayan); Fig. 1 (Yolkin et al., 1994; Shokalsky et al., 2000).

In the last decades a significant progress has been made on the study of the Chinese and Mongolian Altai (Yakubchuk, 2004; Xiao et al., 2010; Wan et al., 2010; Cai et al., 2011; Yarmolyuk et al., 2013; Wu et al., 2015; Chen et al., 2017; Yang et al., 2018; Şengör et al., 2018), but detailed and systematic geochemical and isotope geochronological study is limited for the Rudny Altai one of the largest Devonian polymetallic provinces (Scherba et al., 1998). Some of the sulfide deposits are considered to be an analogue of the "Kuroko" type, i.e. in connection with long-lived hot metal-rich hydrothermal systems of black smokers; whereas others are considered as syngenetic with high temperature subvolcanic felsic intrusions, which were a conductor of heat and fluids and control convection of metal-precipitating hydrothermal flows (Gaskov, 2015). Here we report new geochemical data, zircon U-Pb and Nd isotopic compositions of the subvolcanic rhyolites from the bimodal association from the NW Rudny Altai (Russia) and discuss their petrogenesis, magma sources and geodynamic setting.

2. Tectonic setting and geological framework

The Rudny Altai tectonic block is located on the territory of Russia, Kazakhstan and Chinese Altai, and extends in the North-Western direction for >500 km with a width of about 100 km, in the strip between the North-Eastern regional faults (NEF) and Irtysh Shear Zone (ISZ); Fig. 2a. On the basis of tectonic and volcanic zoning (Kulkov, 1980), its territory is subdivided into five zones: (i) Aley in Russia; (ii–iv) Sinukha-Holzun, Nizhnebukhtarma and Yuzhnoaltai in Eastern Kazakhstan (Bespaev et al., 1997; Scherba et al., 1998); and (v) Ashele in Xinjiang of China (e.g. Wan et al., 2010; Wu et al., 2015; Yang et al., 2018).

Until the start of Devonian volcanism this territory existed as part of the shelf on the margin of the Siberian continent with terrigenous-carbonate sedimentation, similar to the modern passive continental margins (Yolkin et al., 1994). Suggested that the passive margin was "dragged" in the process of Paleozoic drift and rotation of the Siberian continent (Scherba et al., 1998). The Devonian volcano-plutonic belts were formed as a result of the powerful destruction of the Caledonian passive margin, probably on the border of Pragian and Emsian (Rotarash et al., 1982; Scherba et al., 1998). Volcanism developed in the environment of a shallow-sea basin with depths about 0.5 km and not exceeding 1.5 km (Rotarash et al., 1982; Yolkin et al., 1994; Bespaev et al., 1997; Saraev et al., 2012). NW Rudny Altai is represented by the so-called Alei block – the outcrop of the Caledonian deformed basement, with a total size of 200 × 50–60 km. In Early Devonian the Alei Block was subsided and formed a rhomboidal-shaped structure, like pull-apart basin, now looks like half-graben (Fig. 2a). This structure is bounded by the general systems of north-western and sub-latitude faults. The first of them correspond to the ISZ and the NEF zone formed at the stage of formation of the Altai convergent margin, since they control the emplacement of two volcanic belts (Fig. 2c). According to geological mapping at a scale of 1:200,000 (Murzin et al., 2001), these volcanic belts in the sides of the Alei structure were formed synchronously; although it has not yet been determined whether the compositions of volcanic rocks from these belts are identical. The formation of feathering sub-latitudinal faults occurred at the boundary of Givetian and Frasnian (Scherba et al., 1998). In general, based on the structural pattern of the Alei block, it can be argued that the Chara subduction oceanic plate under the Rudny-Altai block was obliquely, WE direction, in modern coordinates. Thus, this differs from the proposed northward subduction of the Junggar plate under the Devonian margin of the Siberian continent (e.g. Xu et al., 2003; Zhang et al., 2018; Ma et al., 2018).

3. Evolution of the volcanism and characteristics of subvolcanic intrusion

3.1. Evolution of the volcanism

The Emsian-Frasnian volcanism was developed in two major stages involving five volcanic rhythms (Fig. 3; Murzin et al., 2001). In this period powerful outbreaks of contrasting predominantly shallow-sea volcanism, accompanied by the injection of subvolcanic and hypabyssal intrusions associated with linear zones of extension; and the formation of numerous polymetallic deposits alternating with partial attenuation stages of volcanic activity (Scherba et al., 1998; Shokalsky et al., 2000; Murzin et al., 2001). The first stage (Late Emsian – Early Givetian) includes two rhythms of felsic volcanism, formed the Melnichno-Sosnovsky (MS) volcanic complex. The first rhythm (Late Emsian – Eifelian) was represented by rare submarine eruptions of felsic lavas and their tuffs, which had minor distribution in comparison with the prevailing fine-grained sedimentary deposits. In contrast, the second rhythm (Early Givetian) was characterized by active eruptions from large volcanoes of the Central-type, and powerful pyroclastic felsic composition deposition, and intrusion of syngenetic subvolcanic rhyolites. The first stage total rock thickness is ~400 m. The second pronounced stage or so-called "Givetian – Frasnian rhyolite-basalt flash" corresponded to the clear mode of extension, and the formation of the so-called Shipunikha rift-like structure in the rear part of the NW Rudny Altai, accompanied by fractured effusions of basalts (Fig. 2a). This stage includes three volcanic rhythms, generally called the third, fourth and fifth. Accordingly, the third rhythm covers the period of formation of the varied stratified strata, consisting of lava, lava-breccia, tuffs and felsic ignimbrites composition (Fig. 3). The fourth rhythm is reflected by the eruptions of basalt flows during the subsidence of the crustal blocks. The fifth rhythm appeared as felsic eruption from numerous volcanoes of the Central-type, inherited on the site of Givetian-Frasnian volcanic structures. With the depletion of magmatic chambers in some areas of the Rudny-Altai block, the subsidence of pre-existing volcanic apparatus and the formation of volcanic-tectonic depressions in their place took place, which, at least until the middle of the Frasnian, maintained a tendency to dive. The total rock thickness is ~450 m. In a first approximation, U-Pb SHRIMP-II age of syngenetic granitoids reveal of the first and second stage: ~395–384 Ma (Kuibida et al., 2015) and ~378–372 Ma (Murzin et al., 2001), respectively. In general, a characteristic feature of volcanism in the NW Rudny Altai was the formation of a contrasting rhyolite-basalt association with the antidromic order of the rhyolites-basalt volcanism in the Emsian-Eifelian; and the pendulum nature of the rhyolite-basalt-rhyolite volcanism in Givetian-Frasnian period. The total volume of felsic volcanism prevailed over the basic volcanism in a ratio of 75:25%; and volcanic products of the intermediate composition were almost absent (Rotarash et al., 1982; Murzin et al., 2001).

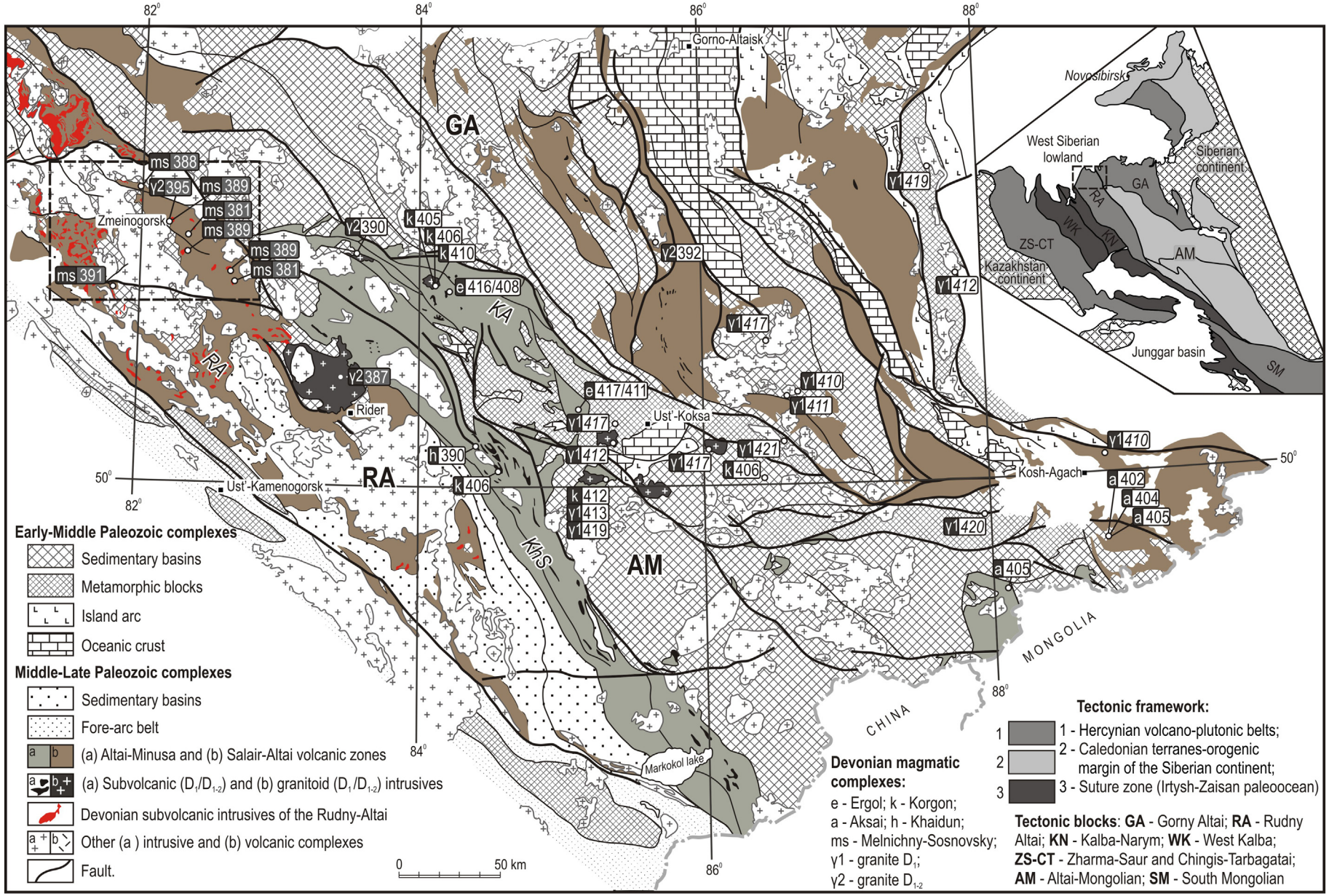

Fig. 1. Structural-geological map of the western part of the Altai accretionary-collision system (Russian Altai) modified after 1:200,000 Geological Maps of the Russian Federation; illustrating the location of the two Devonian volcanic systems (data source from http://www.vsegei.ru/en/geology-of-russia). The tectonic framework is from (Buslov, 2011). Tectonic blocks: RA – Rudny Altai, GA – Gorny Altai (integrated), AM – Altai-Mongolian. Volcanic belts: *RA* – Rudny Altai, *KA* – Korgon-Aksai, *KhS* – Kholzun-Sarymsakty. The numbers in the rectangles indicate the ages (Ma). Normal font (1:200,000 Geological Maps of the Russian Federation (http://www.vsegei.ru/en/geology-of-russia), and (Kuibida et al., 2015; Kuibida, 2019); italic font (Glorie et al., 2011). Ages data for Melnichno-Sosnovsky (MS) volcanic complex is from this study.

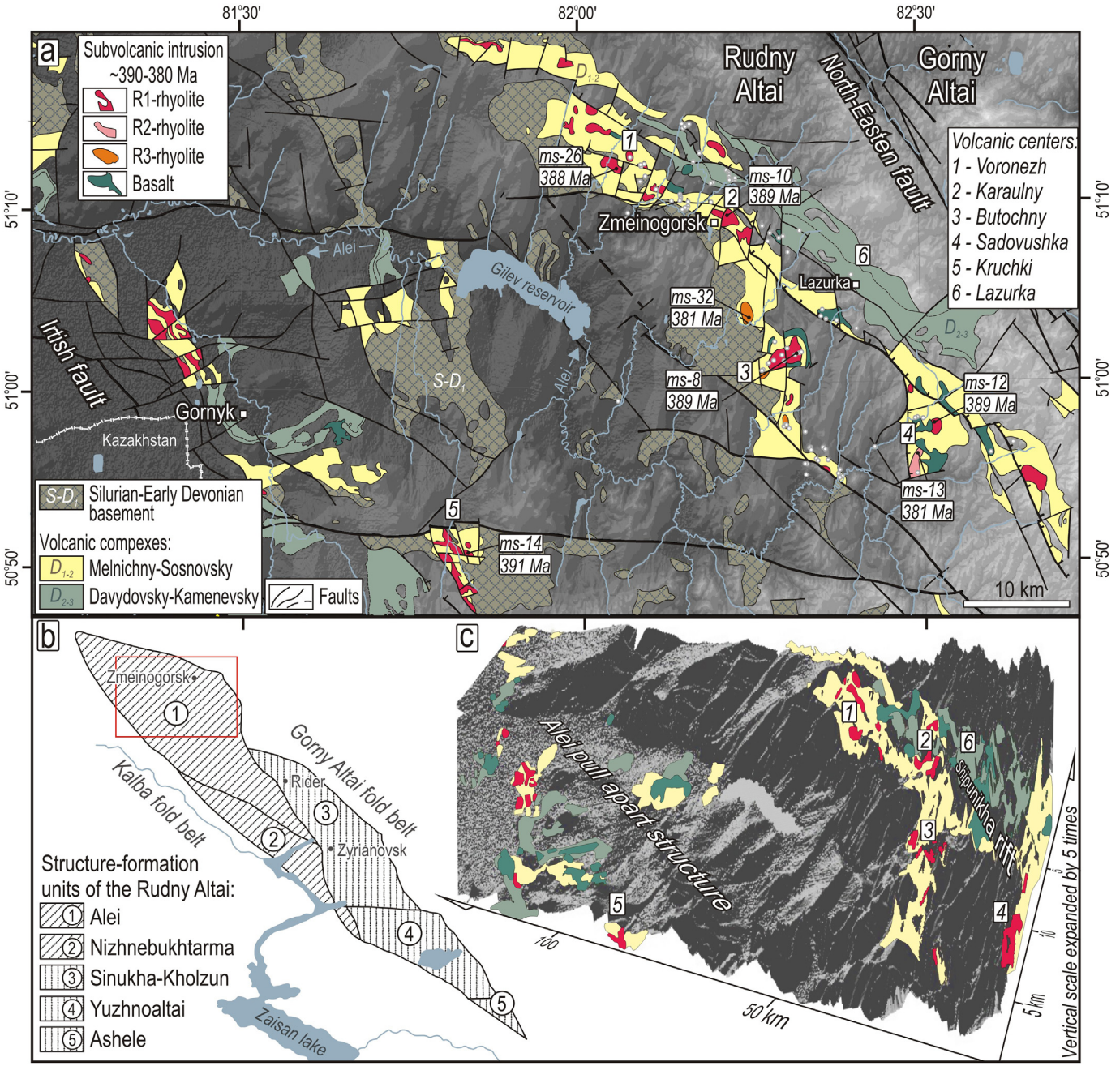

Fig. 2. (a) Shaded relief image (illuminated from the NW), representing the digital elevation model of the NW Rudny Altai, illustrating the location of the two Devonian volcanic belts formed along the NW direction of deformation in the boards of the Alei basement rhomboidal-shaped structure. (b) The principal tectonic scheme of the Rudny Altai, illustrating the division on structure-formation units. (c) Detailed three-dimensional topographic mapping scheme on panel a, illustrating the position Alei structure and Shipunikha rift in structure of NW Rudny Altai. The vertical scale is increased five times.

3.2. Characteristics of subvolcanic intrusion

Subvolcanic MS-rhyolites were collected mainly from the NE volcanic belt (Fig. 2) including several volcanic centers located in a chain on a direction NW-SE: Voronezh, Karaulny, Butochny and Sadovushka (Fig. 4a–h). Butochny and Sadovushka were originally parts of a single volcanic center, but now they are separated by the local pull-apart structure inside the Sipunikha rift (Fig. 2). The volcanic center Kryuchki, the only exposure of MS-rhyolite in the SW volcanic belt, was also collected for this study (Fig. 2). Subvolcanic intrusions occur as stock-, sill- and dike-like bodies localized inside the Late Emsian – Early Givetian stratified volcanogenic-sedimentary deposits of the first stage (Fig. 3). A large number of rhyolites have experienced significant brittle deformations, and are quite often subject to secondary alterations, including limonitization within micro-fracture.

On the basis of field observations, study of thin sections and geochemical compositions we have identified three main types of MS-rhyolites described in this study as R1-, R2- and R3-rhyolites. Rhyolites of the first type compose the main volume of all subvolcanic intrusions in NW Rudny Altai. Rhyolites of the second type are related to the late phases, which form a small-sized subvolcanic body in the frame of the main volcanic edifices. The third type of rhyolite was found only within the Butochniy volcanic center, where they are located, both inside the volcanic structure and in its frame to the North and South.

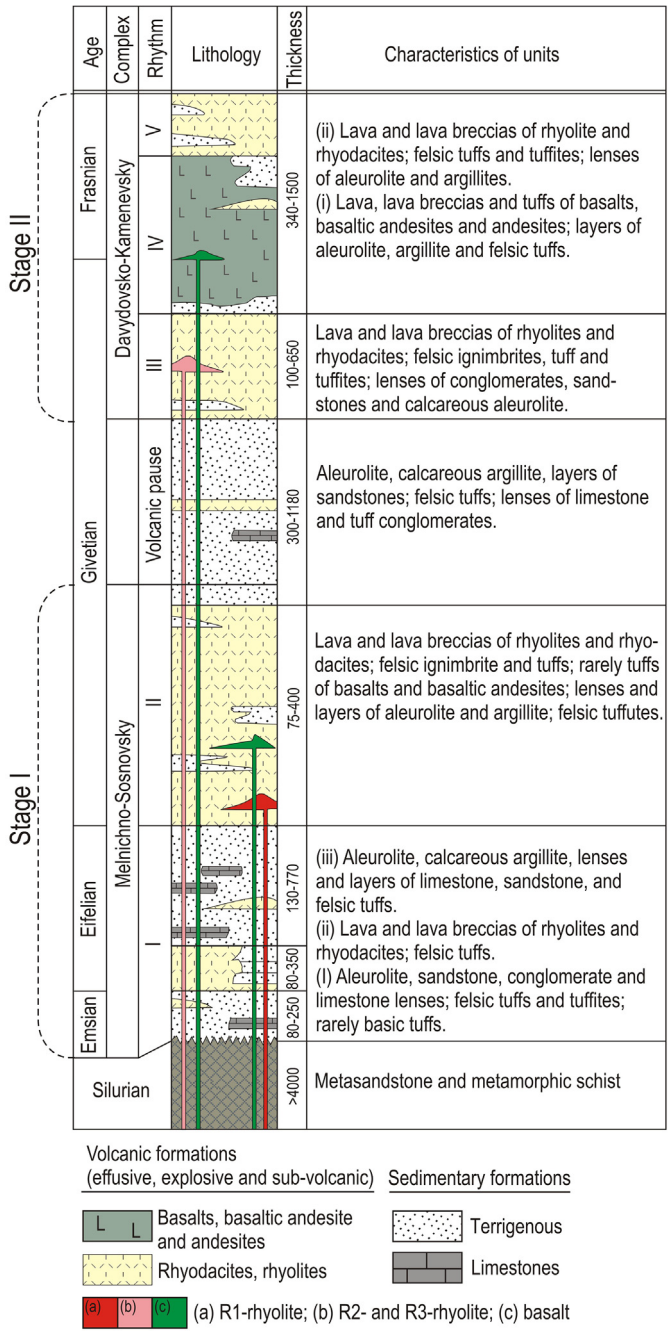

Fig. 3. Stratigraphic columns of end Early Devonian – early Late Devonian volcanic and sedimentary rocks in the NW Rudny Altai (modified from 1:200,000 geological maps (Murzin et al., 2001)), illustrating the two stage evolution of bimodal volcanism, and syngenetic subvolcanic intrusions.

4. Analytical methods

4.1. Zircon U-Pb dating

Zircon separation of an 8 kg rhyolite samples were conducted in the Institute of Geology and Mineralogy by a standard procedure of crushing, panning, heavy liquid and magnetic separation techniques. Zircon grains were hand-picked under a binocular and then mounted in a 20 mm and 6 mm epoxy resin disc. All grains were half-polished to observe the internal structure of zircons at cathodoluminescence (CL) images. The CL imaging was performed at the Novosibirsk Institute Geology and Mineralogy using a Jeol JSM-6510LV scanning electron microscope; and at the University of Tokyo using a JSM-6060VL scanning electron microscope (JEOL, Ltd., Tokyo, Japan) equipped with SSM-7CLS cathodoluminescence (CL) system (Sanyu Electron Co., Ltd., Tokyo, Japan), which was operated at an accelerating voltage of 15 kV. The locations for the spot analysis on zircon grains were selected from CL images and photomicrographs, in transmitted and reflected light, to avoid mineral inclusions and cracks. The CL-images of zircons and the results of $^{206}Pb/^{238}U$ dating are shown in Tables 1, 2 and Figs. 6, 7.

In situ zircon U-Pb datings of MS-10/1 and MS-13/1 samples were conducted by using an Agilent 8800 single-collector triple quadrupole ICP-MS (Agilent Tech., Santa Clara, USA) coupled to a NWR-213 Nd:YAG LA system (ESI, Portland, USA) at the Gakushuin University. The sample discs were set in the two-volume sample chamber of the LA system. The locations for the spot analysis on zircon grains were chosen by referring the CL images and observations with the LA camera to avoid mineral inclusions and cracks. Before the analysis, the locations were ablated using a pulse of laser to remove potential contaminants on the zircon surfaces. At the analysis, they were ablated for 30 s by the laser with fluence of 2.0 J/cm^2, repetition rate of 5 Hz, and laser spot size diameter of 30 μm after laser shooting with laser shutter closed for 30 s (laser warming up). The ablated materials were carried by He gas, which was introduced into the two-volume sample chamber at a flow rate of 0.6 l/min. They were mixed with Ar make-up gas introduced at a flow rate of 1.2 l/min before their introduction into the ICP-MS. On the ICP-MS, 6 nuclides (^{202}Hg, ^{204}Pb, ^{206}Pb, ^{207}Pb, ^{232}Th and ^{238}U) were analyzed. In order to reduce isobaric interference of ^{204}Hg to ^{204}Pb, small amount of mixed ammonia/helium was flowed into collision/reaction cell between the tandem quadropole mass spectrometers (e.g. Kasapoğlu et al., 2016). We succeeded to reduce the blank count on 204 amu ($^{204}Hg + {}^{204}Pb$) <10 cps on average. The background and ablation data for each analysis were collected for 15 s of the laser warming-up time and 20 s of the ablation time, respectively. Those data were acquired for multiple groups of 15 unknown grains bracketed by trio of analyses of the 91500 zircon standard (Wiedenbeck et al., 2004) and NIST SRM610 glass standard. The 91500 was analyzed for correction of elemental fractionation bias of $^{206}Pb/^{238}U$ and Th/U ratios. For the correction, apparent $^{206}Pb/^{238}U$ ratio without common Pb correction by Sakata et al. (2017) and Th/U ratio (Wiedenbeck et al., 2004) were used as normalization values, respectively. The NIST SRM 610 was analyzed for correction of mass fractionation bias of $^{207}Pb/^{206}Pb$ ratios. The isotopic ratio compiled by Jochum and Nohl (2008) was used as a normalization value for the correction. The background intensities collected at the laser warming-up time were subtracted from following signals at the ablations. ^{235}U was calculated from ^{238}U using a $^{238}U/^{235}U$ ratio of 137.88 (Jaffey et al., 1971). The intensity of ^{202}Hg of all analyses was used to correct the isobaric interference of ^{204}Hg on ^{204}Pb. Corrected ^{204}Pb intensities were too low to correct U-Pb ages for common Pb contamination with sufficient precision based on ^{204}Pb (Stern, 1997). Thus, in this study, no common Pb correction was made. All uncertainties of the data are quoted at a 2 sigma level to which repeatability of each six measurements of 91500 zircon and NIST SRM 612 data bracketing unknown sample groups is propagated. Elemental fractionation of U/Pb and Th/U ratios and mass fractionation of $^{207}Pb/^{206}Pb$ ratio were linearly interpolated by the measured data of each six analysis of 91500 zircon and NIST SRM610, respectively. Resulting age interpretations, weighted mean U-Pb ages and Concordia plots were constructed using Isoplot software (Ludwing, 2003). Through all the analyses, Plešovice zircons (Slama et al., 2008) were measured multiple times as secondary standards for quality control. Mean concordia age obtained for Plesovice standard yields $^{206}Pb/^{238}U$ age of 337.2 ± 1.8 Ma (MSWD = 1.0) and $^{207}Pb/^{235}U$ age of 340.2 ± 5.8 Ma (MSWD = 1.2) (n = 25), which is in accordance with the reported ID-TIMS age of 337.1 ± 0.4 Ma (Slama et al., 2008).

For rhyolite samples MS-8, MS-26 and MS-32 the U-Pb geochronological studies were performed by the LA-SF-ICP-MS method on a Thermo Fisher Scientific Element XR high-resolution mass spectrometer

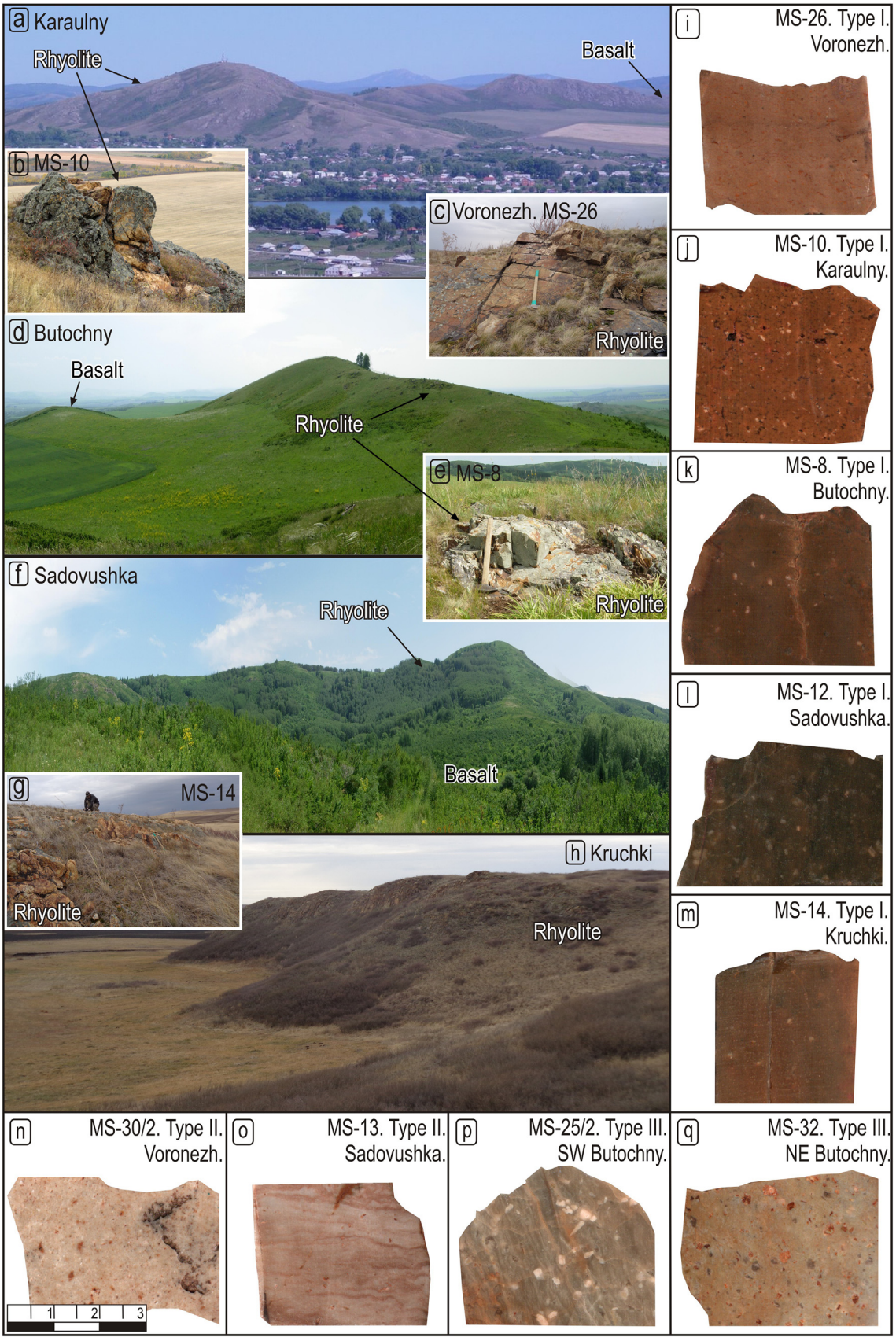

Fig. 4. Representative photos showing survey panoramas of the main volcanic centers and intrusive bodies of MS-rhyolite: (a, b) Karaukny; (c) Voronezh; (c) Butochny (d, e); Kruchki (g, h) of the main petrographic types of volcanic rocks: R1-rhyolite (i–m); R2-rhyolite (n, o); and R3-rhyolite (p, q).

Table 1
LA-ICP-MS zircon U-Pb isotopic data of the Melnichno-Sosnovsky subvolcanic rhyolites (NW Rudny Altai).

Point no	Isotope rations					Ages (Ma)					Concentration (ppm)		
	$^{207}Pb/^{235}U$	2σ	$^{206}Pb/^{238}U$	2σ	Rho	$^{207}Pb/^{235}U$	2σ	$^{206}Pb/^{238}U$	2σ	% conc.	U	Th	Th/U
R1: sample MS-10/1. LA-ICP-MS (Gakushuin University, Japan)													
1	0,45,529	0,00744	0,06103	0,00058	0,58	375,5	30,0	381	5,2	99	397	166	0,42
2	0,45,373	0,00912	0,06134	0,00062	0,5	356,2	39,2	379,9	6,4	94	231	82	0,35
3	0,45,308	0,00866	0,06117	0,00061	0,52	359,4	36,9	379,4	6,1	95	262	84	0,32
4	0,45,311	0,00905	0,06059	0,00061	0,51	381	38,7	379,5	6,3	100	235	78	0,33
5	0,45,132	0,00902	0,06049	0,00061	0,51	375,7	38,8	378,2	6,3	99	236	79	0,34
6	0,45,881	0,00894	0,06075	0,00061	0,51	403	37,4	383,4	6,2	105	248	87	0,35
7	0,45,750	0,00812	0,06092	0,00059	0,55	390,2	33,4	382,5	5,7	102	316	126	0,4
8	0,45,404	0,01064	0,06162	0,00094	0,65	347,7	40,1	380,1	7,4	91	230	82	0,35
9	0,44,859	0,01082	0,06003	0,00109	0,75	379,3	35,6	376,3	7,6	101	301	118	0,39
10	0,46,179	0,01098	0,06003	0,00109	0,76	444,2	34,2	385,5	7,6	115	312	127	0,41
11	0,46,257	0,01340	0,06051	0,00114	0,65	430,3	48,9	386	9,3	111	150	59	0,39
12	0,45,673	0,01062	0,06050	0,00109	0,78	402,1	32,7	382	7,4	105	349	145	0,41
13	0,45,231	0,01122	0,06002	0,00110	0,74	398,4	37,6	378,9	7,8	105	265	91	0,34
14	0,45,656	0,01119	0,06039	0,00110	0,74	405,2	36,6	381,9	7,8	106	276	101	0,37
15	0,45,841	0,01105	0,06094	0,00111	0,75	394	35,5	383,2	7,7	103	294	110	0,37
16	0,45,827	0,01068	0,06188	0,00112	0,78	359,1	33,2	383,1	7,4	94	341	147	0,43
17	0,46,914	0,01126	0,06187	0,00113	0,76	412,2	35,0	390,6	7,8	106	296	122	0,41
18	0,46,250	0,00895	0,06207	0,00062	0,52	373	37,3	386	6,2	97	249	103	0,41
19	0,46,964	0,00940	0,06216	0,00063	0,51	403,8	38,6	390,9	6,5	103	226	84	0,37
20	0,46,789	0,01018	0,06222	0,00094	0,69	393,5	35,2	389,7	7	101	289	108	0,37
21	0,46,751	0,01034	0,06206	0,00094	0,68	397,5	36,1	389,5	7,2	102	273	101	0,37
22	0,46,255	0,00969	0,06237	0,00093	0,71	362,1	33,1	386	6,7	94	334	146	0,44
23	0,46,182	0,01216	0,06198	0,00098	0,6	372,8	47,4	385,5	8,4	97	159	60	0,38
24	0,46,121	0,01085	0,06229	0,00096	0,65	358,6	40,3	385,1	7,5	93	224	77	0,34
25	0,47,375	0,01006	0,06229	0,00094	0,71	418,6	33,5	393,8	6,9	106	312	137	0,44
26	0,46,519	0,01097	0,06124	0,00111	0,77	415,9	33,7	387,9	7,6	107	320	133	0,42
27	0,47,351	0,01009	0,06238	0,00094	0,71	414,3	33,7	393,6	7	105	310	135	0,44
28	0,46,942	0,01088	0,06299	0,00114	0,78	373,1	32,6	390,8	7,5	95	342	142	0,41
R1: sample MS-14/1. LA-ICP-MS (Hong-Kong University)													
1	0,46,905	0,01061	0,06430	0,00120	0,82	390,5	7,3	401,7	7,3	97	413	150	0,36
2	0,46,940	0,00921	0,06265	0,00105	0,85	390,8	6,4	391,7	6,4	99	379	156	0,41
3	0,46,984	0,00938	0,06077	0,00081	0,66	391,1	6,5	380,3	4,9	97	362	198	0,55
4	0,47,001	0,01219	0,06296	0,00073	0,45	391,2	8,4	393,6	4,5	99	404	136	0,34
5	0,46,992	0,00880	0,06018	0,00083	0,73	391,1	6,1	376,7	5,0	96	360	184	0,51
6	0,46,956	0,01283	0,05723	0,00107	0,69	390,9	8,9	358,7	6,5	91	373	183	0,49
7	0,46,928	0,00920	0,06246	0,00091	0,74	390,7	6,4	390,6	5,5	99	360	175	0,49
8	0,47,123	0,01088	0,06140	0,00119	0,84	392,0	7,5	384,1	7,2	97	347	189	0,54
9	0,46,955	0,01412	0,05891	0,00158	0,89	390,9	9,8	369	9,6	94	345	194	0,56
10	0,47,157	0,00893	0,05809	0,00087	0,79	392,3	6,2	364	5,3	92	400	164	0,41
11	0,46,961	0,00882	0,06222	0,00080	0,69	390,9	6,1	389,1	4,9	99	366	180	0,49
12	0,46,813	0,00866	0,06211	0,00087	0,76	389,9	6,0	388,5	5,3	99	350	195	0,56
R1: sample MS-12. LA-ICP-MS (Hong-Kong University)													
1	0,46,726	0,00402	0,06146	0,00047	0,90	389,3	2,8	384,5	2,9	98	345	218	0,63
2	0,46,730	0,00263	0,06246	0,00030	0,85	389,3	1,8	390,6	1,8	99	331	226	0,68
3	0,46,741	0,00366	0,06319	0,00025	0,51	389,4	2,5	395	1,5	98	314	168	0,54
4	0,46,730	0,00276	0,06218	0,00027	0,73	389,3	1,9	388,9	1,6	99	301	249	0,83
5	0,46,792	0,00396	0,06186	0,00022	0,41	389,7	2,7	386,9	1,3	99	342	188	0,55
6	0,46,699	0,00485	0,06135	0,00044	0,69	389,1	3,4	383,8	2,7	98	307	172	0,56
7	0,46,768	0,00267	0,06259	0,00033	0,93	389,6	1,8	391,3	2,0	99	395	194	0,49
8	0,46,743	0,00351	0,06304	0,00037	0,78	389,4	2,4	394,1	2,2	98	400	175	0,44
9	0,46,785	0,00411	0,06232	0,00039	0,71	389,7	2,8	389,7	2,3	99	351	213	0,61
10	0,46,704	0,00225	0,06196	0,00025	0,83	389,1	1,6	387,5	1,5	99	356	220	0,62
11	0,46,757	0,00247	0,06229	0,00029	0,87	389,5	1,7	389,5	1,7	99	349	198	0,57
12	0,46,726	0,00314	0,06106	0,00036	0,89	389,3	2,2	382,1	2,2	98	342	219	0,64
13	0,46,738	0,00291	0,06190	0,00036	0,95	389,4	2	387,2	2,2	99	347	223	0,64
14	0,46,751	0,00414	0,06137	0,00052	0,95	389,5	2,9	384	3,1	98	349	220	0,63
15	0,46,750	0,00383	0,06227	0,00046	0,91	389,5	2,6	389,4	2,8	99	409	186	0,45
R1: sample MS-26. LA-ICP-MS (IGM SB RUS, Novosibirsk, Russia)													
1	0,46,573	0,01189	0,06158	0,00102	0,65	388,2	8,2	385,2	6,2	100	141	310	0,45
2	0,46,575	0,01104	0,06190	0,00102	0,70	388,2	7,7	387,2	6,2	99	190	351	0,54
3	0,46,305	0,01423	0,06173	0,00105	0,55	386,4	9,9	386,2	6,4	99	136	167	0,81
4	0,48,381	0,01101	0,06195	0,00102	0,72	400,7	7,5	387,5	6,2	102	535	635	0,84
5	0,47,126	0,01209	0,06180	0,00103	0,65	392,1	8,3	386,6	6,2	100	209	388	0,54
6	0,46,576	0,00873	0,06236	0,00101	0,86	388,3	6,1	390	6,1	101	804	1183	0,68
7	0,46,450	0,01172	0,06195	0,00103	0,66	387,4	8,1	387,5	6,3	99	213	301	0,71
8	0,46,715	0,01114	0,06173	0,00102	0,69	389,2	7,7	386,2	6,2	100	580	546	1,06
9	0,46,638	0,01228	0,06195	0,00104	0,64	388,7	8,5	387,4	6,3	99	139	263	0,53
10	0,48,012	0,01191	0,06195	0,00103	0,67	398,2	8,2	387,5	6,3	102	298	462	0,65
11	0,46,822	0,01068	0,06188	0,00102	0,72	390	7,4	387,1	6,2	100	505	472	1,07
12	0,48,308	0,01199	0,06230	0,00104	0,67	400,2	8,2	389,6	6,3	102	282	352	0,80
13	0,47,824	0,01145	0,06205	0,00103	0,69	396,9	7,9	388,1	6,3	101	356	426	0,84

Table 1 (*continued*)

Point no	Isotope rations					Ages (Ma)					Concentration (ppm)		
	$^{207}Pb/^{235}U$	2σ	$^{206}Pb/^{238}U$	2σ	Rho	$^{207}Pb/^{235}U$	2σ	$^{206}Pb/^{238}U$	2σ	% conc.	U	Th	Th/U
14	0,46,902	0,01359	0,06227	0,00106	0,59	390,5	9,4	389,4	6,4	99	147	249	0,59
15	0,46,591	0,01697	0,06212	0,00109	0,48	388,4	11,8	388,5	6,6	99	64	108	0,59
16	0,46,814	0,01071	0,06243	0,00103	0,72	389,9	7,4	390,4	6,3	101	412	530	0,78
17	0,46,621	0,01080	0,06193	0,00102	0,71	388,6	7,5	387,3	6,2	99	278	388	0,72
18	0,46,946	0,01219	0,06193	0,00104	0,65	390,8	8,4	387,3	6,3	100	360	412	0,87
19	0,46,917	0,01027	0,06229	0,00103	0,76	390,6	7,1	389,5	6,2	99	631	731	0,86
20	0,48,887	0,01164	0,06229	0,00103	0,69	404,1	7,9	389,5	6,3	103	399	456	0,87
21	0,46,917	0,01244	0,06191	0,00104	0,63	390,6	8,6	387,2	6,3	100	248	326	0,76
22	0,46,810	0,01115	0,06227	0,00103	0,69	389,9	7,7	389,4	6,3	99	353	463	0,76
23	0,50,836	0,02233	0,06194	0,00113	0,42	417,3	15	387,4	6,9	107	68	114	0,6
24	0,46,832	0,01290	0,06172	0,00104	0,61	390	8,9	386,1	6,3	100	359	404	0,89
25	0,47,093	0,01302	0,06269	0,00106	0,61	391,8	9	392	6,4	101	193	300	0,64
26	0,46,615	0,01374	0,06167	0,00105	0,58	388,5	9,5	385,8	6,4	100	122	220	0,56
27	0,46,536	0,01563	0,06183	0,00107	0,52	388	10,8	386,8	6,5	99	241	193	1,25
28	0,46,769	0,01558	0,06199	0,00107	0,52	389,6	10,8	387,7	6,5	99	125	172	0,73
29	0,49,424	0,01643	0,06189	0,00107	0,52	407,8	11,2	387,1	6,5	104	161	215	0,75
30	0,46,573	0,01174	0,06220	0,00104	0,66	388,2	8,1	389	6,3	101	204	399	0,51
31	0,48,378	0,01556	0,06198	0,00107	0,54	400,7	10,7	387,6	6,5	102	115	254	0,45
32	0,46,449	0,01137	0,06197	0,00104	0,69	387,4	7,9	387,6	6,3	101	192	319	0,6
33	0,46,919	0,01373	0,06254	0,00107	0,58	390,6	9,5	391,1	6,5	101	305	418	0,73
34	0,48,080	0,01550	0,06229	0,00108	0,54	398,6	10,6	389,5	6,6	101	152	199	0,76
35	0,46,409	0,01281	0,06199	0,00105	0,61	387,1	8,9	387,7	6,4	101	98	273	0,36
36	0,46,771	0,01133	0,06241	0,00105	0,69	389,6	7,8	390,2	6,4	101	226	403	0,56
37	0,48,443	0,01621	0,06222	0,00109	0,52	401,1	11,1	389,1	6,6	102	209	330	0,63
R1: sample MS-8. LA-ICP-MS (IGM SB RUS, Novosibirsk, Russia)													
1	0,46,279	0,01488	0,06178	0,00118	0,59	386,2	10,3	386,4	7,2	100	358	122	0,34
2	0,47,005	0,01461	0,06242	0,00119	0,61	391,2	10,1	390,3	7,2	100	317	135	0,43
3	0,46,202	0,01212	0,06154	0,00115	0,71	385,7	8,4	385	7,0	100	350	149	0,42
4	0,47,220	0,01654	0,06207	0,00119	0,55	392,7	11,4	388,2	7,2	101	253	85	0,34
5	0,46,907	0,01394	0,06209	0,00117	0,63	390,5	9,6	388,3	7,1	101	312	112	0,36
6	0,46,449	0,01861	0,06192	0,00122	0,49	387,4	12,9	387,3	7,4	100	254	78	0,31
7	0,46,955	0,01258	0,06237	0,00116	0,69	390,9	8,7	390,1	7,1	100	428	167	0,39
8	0,46,773	0,01666	0,06224	0,0012	0,54	389,6	11,5	389,2	7,3	100	535	175	0,33
9	0,46,433	0,01671	0,06196	0,00119	0,53	387,3	11,6	387,5	7,2	100	394	130	0,33
10	0,46,949	0,01384	0,06201	0,00116	0,63	390,8	9,6	387,8	7,1	101	362	174	0,48
11	0,46,945	0,01762	0,06196	0,00119	0,51	390,8	12,2	387,6	7,2	101	159	56	0,36
12	0,47,301	0,01362	0,06258	0,00117	0,65	393,3	9,4	391,3	7,1	101	386	203	0,73
13	0,47,170	0,01249	0,06274	0,00116	0,7	392,4	8,6	392,3	7,1	100	429	224	0,64
14	0,47,388	0,01866	0,06252	0,00122	0,5	393,9	12,9	391	7,4	100,7	263	139	0,52
15	0,46,299	0,01145	0,06178	0,00114	0,75	386,3	8	386,4	6,9	100	352	282	0,73
16	0,47,212	0,01301	0,06231	0,00116	0,68	392,7	9	389,6	7,1	100,8	249	147	0,62
17	0,46,870	0,01307	0,06239	0,00116	0,67	390,3	9	390,1	7,1	100,1	530	412	0,54
R2: sample MS-13. LA-ICP-MS (Gakushuin University, Japan)													
1	0,47,126	0,01564	0,06116	0,00125	0,61	392,1	10,8	382,7	7,6	102	128	40	0,31
2	0,45,028	0,01411	0,05945	0,00119	0,64	377,5	9,9	372,3	7,2	101	154	58	0,37
3	0,44,671	0,01211	0,05939	0,00115	0,71	375	8,5	371,9	7,0	101	261	126	0,48
4	0,48,640	0,01486	0,06160	0,00123	0,66	402,5	10,1	385,4	7,5	104	153	56	0,37
5	0,47,731	0,01638	0,06299	0,00186	0,86	396,2	11,3	393,8	11,3	101	247	78	0,32
6	0,45,552	0,01577	0,06087	0,00180	0,85	381,1	11,0	380,9	10,9	100	241	98	0,41
7	0,48,376	0,01635	0,06182	0,00182	0,87	400,7	11,2	386,7	11,1	104	272	133	0,49
8	0,46,729	0,01498	0,06268	0,00183	0,91	389,3	10,4	391,9	11,1	99	466	177	0,38
9	0,52,926	0,01695	0,06342	0,00186	0,91	431,3	11,3	396,4	11,2	109	422	264	0,62
10	0,46,994	0,01565	0,06269	0,00184	0,88	391,1	10,8	392	11,2	100	316	132	0,42
11	0,48,584	0,01618	0,06294	0,00185	0,88	402,1	11,1	393,5	11,2	102	306	152	0,5
12	0,46,730	0,01523	0,06264	0,00183	0,9	389,3	10,5	391,7	11,1	99	386	203	0,52
13	0,46,369	0,01498	0,06202	0,00181	0,91	386,8	10,4	387,9	11,0	100	429	224	0,52
14	0,52,450	0,01644	0,06466	0,00189	0,93	428,2	10,9	403,9	11,4	569	569	344	0,6
15	0,50,739	0,01616	0,06777	0,00198	0,92	416,7	10,9	422,7	12,0	463	463	380	0,82
16	0,52,978	0,01784	0,06797	0,00200	0,87	431,7	11,8	423,9	12,1	257	257	86	0,34
R3: sample MS-32. LA-ICP-MS (IGM SB RUS, Novosibirsk, Russia)													
1	0,46,943	0,00985	0,06275	0,00106	0,81	390,8	6,8	392,3	6,4	106	537	154	0,29
2	0,51,548	0,01000	0,06294	0,00105	0,86	422,1	6,7	393,5	6,4	106	2567	933	0,36
3	0,45,145	0,01158	0,06074	0,00103	0,66	378,3	8,1	380,2	6,3	129	447	146	0,33
4	0,49,630	0,01041	0,06315	0,00105	0,79	409,2	7,1	394,8	6,4	111	2068	1172	0,57
5	0,45,193	0,00911	0,05930	0,00097	0,81	378,6	6,4	371,4	5,9	108	3858	1310	0,34
6	0,49,839	0,01000	0,06171	0,00101	0,82	410,6	6,8	386	6,2	110	3578	1911	0,53
7	0,48,221	0,00893	0,06405	0,00107	0,9	399,6	6,1	400,2	6,5	94	2980	1298	0,44
8	0,48,426	0,01312	0,06407	0,00111	0,64	401	8,98	400,3	6,71	100,2	303	181	0,6
9	0,48,221	0,00893	0,06405	0,00107	0,9	399,6	6,12	400,2	6,5	99,9	2980	1298	0,44
10	0,48,995	0,01216	0,06485	0,00111	0,69	404,9	8,28	405,1	6,7	100	390	185	0,48
11	0,49,264	0,00932	0,06487	0,00108	0,88	406,7	6,34	405,2	6,56	100,4	2140	867	0,41
12	0,49,777	0,00956	0,06512	0,00109	0,87	410,2	6,48	406,7	6,58	100,9	2840	839	0,3

(*continued on next page*)

Table 1 (*continued*)

Point no	Isotope rations					Ages (Ma)					Concentration (ppm)		
	$^{207}Pb/^{235}U$	2σ	$^{206}Pb/^{238}U$	2σ	Rho	$^{207}Pb/^{235}U$	2σ	$^{206}Pb/^{238}U$	2σ	% conc.	U	Th	Th/U
13	0,49,483	0,00935	0,06512	0,00108	0,88	408,2	6,35	406,7	6,56	100,4	2686	1337	0,5
14	0,52,103	0,01114	0,06498	0,00109	0,78	425,8	7,44	405,8	6,57	104,9	2155	747	0,35
15	0,49,852	0,01566	0,06476	0,00112	0,55	410,7	10,61	404,5	6,8	101,5	255	98	0,38
16	0,49,509	0,00941	0,06484	0,00107	0,87	408,4	6,39	405	6,49	100,8	3129	875	0,28
17	0,50,803	0,01038	0,06485	0,00107	0,81	417,1	6,99	405	6,47	103	2459	671	0,27
18	0,49,917	0,00979	0,06473	0,00106	0,83	411,1	6,63	404,3	6,44	101,7	3436	1186	0,35
19	0,49,018	0,00969	0,065	0,00107	0,83	405	6,6	405,9	6,45	99,8	3578	1911	0,32
20	0,49,736	0,01013	0,06468	0,00106	0,8	409,9	6,87	404	6,43	101,5	3217	1068	0,33

with a New Wave Research UP-213 laser ablation system, at the Institute of Geology and Mineralogy (Russia, Novosibirsk). The analysis was applied to 20–50 single zircon grains, similar in morphology and size in each sample, which were embedded in epoxy resin together with Temora (Black et al., 2004) and Plešovice (Slama et al., 2008) standard zircons. The zircon grains were cut off to about a half of their thickness and polished. The dating points on the grain surfaces were selected using BSE and CL images. Signal was tuned to maximum sensitivity for Pb and U while keeping oxide production, monitored as $^{254}UO/^{238}U$, well below 2% by ablation of NIST SRM 612 glass. The laser was operated at 5 Hz using a spot size of 30 μm and a laser fluence of ~3 J/cm^2. Data were acquired for masses 202–204–206–207–208–232–235–238 in low-resolution E-scan mode during a 25 s background measurement followed by a 30 s sample ablation. The evaporated particles were carried from the laser system to the mass spectrometer in a stream of pure He. Data reduction was carried out using the "Glitter" software package (Griffin et al., 2008). The laser induced elemental fractionation and mass bias was corrected by normalizing the data to the Temora reference zircon (Black et al., 2004). Resulting age interpretations, weighted mean U-Pb ages and Concordia plots were constructed using Isoplot software (Ludwing, 2003). All uncertainties reported are standard deviations at the 1-sigma confidence-level. The Plešovice (Slama et al., 2008) zircon standard was measured multiple times throughout each sequence as an unknown for accuracy check. Mean concordia age obtained for Plesovice standard yields 337.5 ± 3 Ma (n = 12), which is in accordance with the reported ID-TIMS age of 337.1 ± 0.4 Ma (Slama et al., 2008).

For rhyolite samples MS-12 and MS-14 the U-Pb isotopic compositions of zircon grains were analyzed on a VG PQ Excell ICP-MS equipped with a NewWave Research UV213 laser ablation system in the Department of Earth Sciences, the University of Hong Kong. The laser system delivers a beam of 213 nm UV light from a frequency quintupled Nd: YAG laser. Most analyses were carried out with a beam diameter of 30 μm, at a 6 Hz repetition rate. This gave a ^{238}U signal of 3 × 104 to 200 × 104 counts per second, depending on U contents. Typical ablation time was 30–60 s, resulting in pits 20- to 40-μm-deep. Before measurement, samples were ablated for 10 s to eliminate common lead contamination on sample surfaces. In addition, ^{202}Hg was monitored to control the isobaric interference of ^{204}Hg on ^{204}Pb. Data acquisition started with a 15 s measurement of a gas blank during the laser warm-up time. The ^{204}Pb signal was so small that the common lead correction is therefore regarded as unnecessary (Xia et al., 2004). The standard zircon 91500 was used to evaluate the magnitude of mass bias and inter-elemental fractionation. The instrumental settings and detailed analytical procedures are described in Xia et al. (2004). The U-Pb ages were calculated using the U decay constants of 238 U = 1.55125×10^{-10} year^{-1}, $^{235}U = 9.8454 \times 10^{-10}$ year^{-1} and the Isoplot 3 software (Ludwing, 2003). Individual analyses are presented with 1σ errors, and uncertainties in pooled age results are quoted at the 95% confidence level (2σ).

4.2. Whole-rock compositions

The concentrations of major elements were measured by a CMP-25 Xray fluorescence (XRF) device according to the state standard of the USSR Ministry of Geology (GOST 41-08-212-82) at the Institute of Geology and Mineralogy (IGM, Novosibirsk). Trace elements were determined by the inductively coupled plasma mass spectrometry (ICP-MS) on a Finnigan Element ICP-MS analyzer, at IGM, following the protocols of Jenner et al. (1990). Powdered samples were digested in a HF-HNO3 (2:1) mixture in a screw-top Teflon beaker for 2 days at ~100 °C, then evaporated to dryness, refluxed in 6 N HCl and dried twice, and then redissolved in 1 N HCl. The procedure was repeated till complete dissolution of the powder. The final solution was evaporated to dryness, refluxed in 6 N HNO3, dried three times, and dissolved in 2% HNO3. The wet chemistry analytical work was conducted under clean lab conditions. The precision and accuracy of the analyses were checked against the BHVO-1 (Jenner et al., 1990), BCR-1 (Jochum and Nohl, 2008), and JB-3 (Orihashi and Hirata, 2003) international standards and estimated to be 2–7% for rare earth and high-field strength elements. The element abundances and ratios were normalized to chondritic (e.g., La/Sm_n) and primitive mantle (PM) values (e.g., Th/Nb_{pm}), with reference to Sun and McDonough (1989) and McDonough et al. (1992), respectively. Representative analyses of major and trace element contents (in wt% and ppm, respectively) are given in Table 3.

4.3. Isotopes

Radiogenic Sm-Nd isotope studies were carried out for bulk samples at the Geological Institute of the Kola Science Center (Apatity) on a Finnigan MAT 262 (RPQ) seven-channel solid-state mass spectrometer. Isotope ratios were normalized to $^{146}Nd/^{144}Nd = 0.7219$ and then recalculated for the $^{143}Nd/^{144}Nd = 0.511860$ ratio assumed for the La Jolla Nd standard, with a $^{143}Nd/^{144}Nd$ weight average ratio of 0.511837 ± 12 (2σ), from 36 measurements. The εNd(t) values and model ages T_{DM} were calculated with reference to $^{143}Nd/^{144}Nd = 0.512638$ and $^{147}Sm/^{144}Nd = 0.1967$ (Jacobsen and Wasserburg, 1984) and the respective depleted mantle (DM) ratios of $^{143}Nd/^{144}Nd = 0.513151$ and $^{147}Sm/^{144}Nd = 0.2136$ (Goldstein and Jacobsen, 1988). Two-stage age models T_{DM-2} were obtained assuming a middle crust ratio of $^{147}Sm/^{144}Nd = 0.12$ (Liew and Hofmann, 1998). Sm-Nd isotopic data are presented in Table 3; all errors quoted in this paper are 2σ. All the εNd(t) values of the R1-rhyolites, and R2 and R3-rhyolites have been calculated using the average U-Pb age of 390 and 380 Ma, respectively.

5. Results

5.1. Petrography and mineralogy

The R1-type is mainly a porphyry rhyolite, rarely aphyric, commonly yellowish, sometime mauve or reddish. They have a massive, sometimes striped texture, where discontinuous strips and lenses are composed of spherulites (Fig. 5a–e). Within the same subvolcanic intrusions of porphyritic varieties the central parts can be oligophyric and aphyric. Phenocrysts of quartz and alkaline feldspar (from 0.2 to 2 mm) make up 1–2 to 10–40% of the rock volume. Quartz forms isometric grains with melted edges; plagioclases are represented by

Table 2
Major oxides (wt%) and trace elements (ppm) in the MS-rhyolites.

Volcanic center	Voronezh								Karaulny		Butochny		
Phase	1	1	1	1	1	1	1	1	1	1	1	1	1
№	ms-25/2	ms-25/4	ms-26	ms-30/1	ms-4/1	ms-4/2	ms-4/4	ms-4/5	ms-10/1	ms-10/3	ms-6	ms-8	ms-15
SiO_2	76.73	78.87	86.3	77.26	78.99	76.93	79.45	81.7	76.42	77.48	79.32	79.12	77.09
TiO_2	0.22	0.13	0.15	0.17	0.17	0.18	0.14	0.02	0.16	0.1	0.02	0.04	0.13
Al_2O_3	12.47	12	8.59	12.57	11.67	12.38	11.68	10.95	12.22	12.11	10.42	11.47	12.12
Fe_2O_3*	3.1	1.6	1.61	2.61	1.69	3.23	1.56	1.05	3.02	3.03	3.15	2.3	3.65
MnO	0.06	0.04	0.01	0.07	2.26	1.58	1.51	0.01	0.02	0.03	0.02	0.01	0.05
MgO	0.86	0.42	0.49	0.34	0.05	0.06	0.02	0.86	0.29	0.19	0.09	0.06	0.29
CaO	0.27	0.2	0.1	0.29	0.21	0.15	0.14	0.1	0.08	0.25	0.05	0.05	0.16
Na_2O	3.83	3.83	0.18	4.8	4.82	3.64	2.6	4.57	3.79	3.78	3.41	4.27	2.75
K_2O	2.41	2.9	2.53	1.86	0.12	1.83	2.88	0.73	3.96	3.01	3.5	2.67	3.74
P_2O_5	0.04	0.02	0.04	0.03	0.01	0.02	0.01	0.01	0.04	0.03	0.02	0.02	0.02
LOI	1.35	0.9	1.87	1.15	1.34	1.98	1.59	0.97	1	0.92	0.38	0.59	1.34
Th	6.85	8.7	6.09	5.62	6.9	8.85	9.07	8.63	6.43	7.42	6.41	7.87	6.92
U	2.56	2.64	2.16	2.19	3.96	2.9	2.71	2.41	2.8	2.8	2.52	2.77	2.66
Ga	11	12	12	15	8	19	15	10	13	12	9	12	15
Rb	32	42	63	39	29	53	61	29	35	45	64	45	97
Ba	834	1286	388	338	220	594	572	205	283	406	694	520	443
Cs	0.11	0.19	0.65	0.37	0.11	0.47	0.43	0.22	0.11	0.11	0.26	0.22	0.67
Sr	107	111	14	88	56	58	52	74	53	223	65	74	181
La	32.1	37.8	25.4	21.4	25	20	22.8	30.1	47.8	25.4	28.7	19.7	30
Ce	62	66	55	51	49	40	49	62	110	49	56	33	56
Pr	7.9	9.1	6.8	5.5	6.8	5.6	6.9	7.9	11.5	7	6.9	5.4	6.9
Nd	31.2	35.6	28	22	26.1	20.9	25.6	27.9	45.5	25.1	26.9	19.1	26.9
Sm	7.7	8.1	5.9	5.1	5.7	4.9	5.7	5.4	10.5	5.4	6.1	4.3	6.3
Eu	1.3	0.99	1.08	1.25	1.22	1.08	0.86	0.81	1.43	1.3	1.07	1.08	1.19
Gd	7.7	8.56	5.5	4.92	6.76	6	6.14	5.53	10.22	5.94	6.01	4.53	6.78
Tb	1.29	1.48	0.9	0.84	1.26	1.14	1.17	0.96	1.53	1.05	1.05	0.87	1.24
Dy	7.54	9.23	5.45	5.17	8.22	7.63	7.58	5.84	8.94	6.42	6.44	5.78	7.06
Ho	1.7	1.93	1.14	1.14	1.6	1.65	1.65	1.22	1.79	1.33	1.3	1.22	1.56
Er	4.74	5.68	3.2	3.6	4.82	4.97	5.09	3.66	4.68	3.78	3.78	3.84	4.49
Tm	0.81	0.94	0.47	0.56	0.74	0.82	0.83	0.6	0.76	0.57	0.59	0.65	0.68
Yb	5.06	5.84	3.2	3.9	4.73	5.43	5.2	3.96	4.82	3.76	4.05	4.24	4.57
Lu	0.8	0.88	0.47	0.6	0.72	0.84	0.83	0.6	0.74	0.6	0.6	0.66	0.68
Zr	247	180	148	183	213	273	207	109	182	172	207	199	242
Hf	6.69	5.53	4.04	4.9	5.22	6.6	5.52	3.52	5.39	4.45	5.58	5.18	6.19
Ta	0.63	0.81	0.74	0.59	0.69	0.82	0.86	0.82	0.75	0.63	0.63	0.63	0.63
Nb	8.3	8.9	10	8.4	10.8	13	12.9	11.8	9.9	9.2	8	9.9	8.9
Y	48	56	31	32	57	56	49	34	50	42	37	38	46
V	1.2	0.4	10.4	1.2	15.9	69	0.4	17.1	1	0.4	0.9	28.8	0.7
Cr	13	17	25	20	12	17	–	9	10	28	112	8	70
Co	1.4	0.9	1.2	0.8	–	–	–	–	0.9	1.2	1.7		1.1
Ni	–	–	10	9	53	–	–	59	29	37	36	45	39
Pb	7	9	3	11	17	12	2	4	12	6	4	4	7
Cu	29	45	16	16	20	16	17	19	17	20	25	17	18
Zn	170	173	26	80	187	108	66	29	93	93	77	77	84
Eu/Eu*	0.5	0.4	0.6	0.8	0.6	0.6	0.4	0.4	0.4	0.7	0.5	0.7	0.6
La/Yb_n	4	4	5	4	4	2	3	5	7	5	5	3	4
Sr/Y	2.2	2	0.5	2.7	1	1	1.1	2.2	1.1	5.4	1.8	1.9	3.9
ΣРЗЭ	172	192	143	127	143	121	139	157	260	137	150	104	154

Volcanic center	Sadovushka			Kruchki			Sadovushka	Voronezh	Butochny				
Phase	1	1	1	1	1	1	2	2	2	3	3	3	3
№	ms-1/2	ms-1/3	ms-12	ms-14/1	ms-14/2	ms-14/3	ms-13/1	ms-30/2	ms-16	ms-17	ms-19	ms-22	ms-32
SiO_2	76.2	75.53	77.17	79.1	76.21	76.44	78.1	84.95	77.41	77.8	78.22	78.53	82.68
TiO_2	0.15	0.21	0.19	0.11	0.17	0.13	0.02	0.06	0.11	0.04	0.03	0.06	0.04
Al_2O_3	12.38	12.34	12.51	10.44	12.06	12.35	11.93	8.28	11.42	12.2	11.69	11.8	9.52
Fe_2O_3*	1.54	2.19	2.46	1.48	2.38	2.29	1.88	1.94	2.19	1.89	1.81	0.84	1.34
MnO	0.52	0.22	0.54	0.02	0.03	0.03	0.02	0.02	0.01	0.01	0.02	0.02	0.02
MgO	0.01	0.01	0.02	0.26	0.41	0.49	2.02	0.13	0.08	0.18	0.05	0.14	0.35
CaO	0.19	0.15	0.27	0.93	1.17	0.4	0.79	0.2	0.05	0.05	1.35	0.07	0.1
Na_2O	1.28	1.63	4.56	1.33	3.23	4.14	3.34	4.17	0.14	1.97	2.65	1.3	0.12
K_2O	7.72	7.71	2.26	6.31	4.33	3.7	1.87	0.22	8.58	5.84	4.15	7.24	5.81
P_2O_5	0.01	0.01	0.01	0.02	0.02	0.02	0.03	0.02	0.01	0.02	0.02	0.02	0.02
LOI	0.2	0.82	0.72	0.38	0.52	0.77	2.03	0.46	0.69	0.88	0.54	0.43	1.07
SUM	100	100	100	100	100	100	100	100	100	100	100	100	100
Th	11.8	7.81	9.48	7.78	8.4	7.66	9.41	4.58	6.64	9.62	8.64	9.03	7.48
U	3.39	2.51	3.04	3.13	3.47	3.1	2.63	1.66	2.77	3.08	3.42	5	2.65
Ga	8	23	21	10	19	20	12	4	9	13	16	13	9
Rb	98	27	57	64	42	45	190	5	90	136	80	141	99
Ba	450	238	333	583	410	534	864	125	732	656	816	417	639
Cs	0.4	0.25	0.19	0.24	0.2	0.49	1.57	0.11	0.52	1.6	0.75	0.78	0.45

(continued on next page)

Table 2 (*continued*)

Volcanic center	Sadovushka			Kruchki			Sadovushka	Voronezh	Butochny				
Phase	1	1	1	1	1	1	2	2	2	3	3	3	3
№	ms-1/2	ms-1/3	ms-12	ms-14/1	ms-14/2	ms-14/3	ms-13/1	ms-30/2	ms-16	ms-17	ms-19	ms-22	ms-32
Sr	33	36	35	129	158	112	41	96	50	79	144	69	21
La	27.5	24	42.5	26.1	40.8	32.2	18.3	15.4	19.2	19.9	22.7	23.6	13.5
Ce	56	57	81	65	85	71	34	30	37	41	41	40	32
Pr	7.9	8.9	10.5	8.3	10.4	9	4	3.4	4.3	5.2	5.5	5.7	3.7
Nd	28.7	36.1	40.4	32.3	42	38.3	15	12.7	16	20	20.9	21.6	15.1
Sm	6.8	8.7	9.4	7.4	9.3	9.7	3.1	2.7	3.4	5	5.3	5.6	3.7
Eu	0.9	1.63	1.36	0.83	1.51	2.07	0.44	0.27	0.28	0.31	0.47	0.37	0.26
Gd	6.93	9.89	10.4	6.92	9.12	9.93	3.54	2.75	3.57	4.65	5.21	6.48	3.79
Tb	1.32	1.89	1.72	1.1	1.57	1.69	0.67	0.5	0.68	0.72	0.93	1.2	0.7
Dy	8.36	12.17	10.9	6.93	9.67	9.78	4.73	3.41	4.07	3.86	5.35	7.45	4.56
Ho	1.8	2.58	2.36	1.44	2.17	1.97	1.08	0.75	0.91	0.84	1.14	1.62	0.97
Er	5.44	7.95	6.73	4.08	6.94	5.48	3.17	2.2	2.53	2.4	3.2	4.47	2.82
Tm	0.91	1.28	1.1	0.68	1.21	0.87	0.48	0.34	0.4	0.38	0.51	0.72	0.45
Yb	5.86	8.26	7.24	4.6	8.15	6.4	3.2	2.24	2.77	2.31	3.36	4.57	3.1
Lu	0.9	1.26	1.11	0.69	1.18	0.94	0.51	0.33	0.4	0.36	0.51	0.71	0.47
Zr	217	378	245	179	265	249	171	56	59	78	68	72	59
Hf	6.25	9.46	7.93	6.08	8.25	7.08	5.04	1.78	2.3	3.22	2.98	3.07	2.4
Ta	0.73	0.82	0.81	0.77	0.77	0.77	0.66	0.55	0.78	1.22	1.14	1.2	0.77
Nb	10.9	15.3	9	11.7	12.8	11	7.3	6.7	8.2	13.4	11.6	12.1	10.4
Y	52	77	73	31	53	50	30	26	25	21	31	48	27
V	32.3	23	1	3.8	3.1	1.9	3	3.7	1.1	2.1	0.8	0.7	1.5
Cr	15	16	25	54	33	19	22	60	59	582	29	31	44
Co	–	–	0.4	2	1.5	0.8	0.5	1.6	1.5	4.9	1	1.1	1.5
Ni	11	54	39	30	16	10	23	39	28	64	8	21	22
Pb	10	9	7	6	9	5	3	20	4	12	14	16	5
Cu	16	19	18	18	18	18	29	24	19	32	14	19	17
Zn	30	115	82	9	42	80	56	15	30	2048	44	29	28
Eu/Eu*	0.4	0.5	0.4	0.3	0.5	0.6	0.4	0.3	0.2	0.2	0.3	0.2	0.2
La/Yb_n	3	2	4	4	3	3	4	5	5	6	5	3	3
Sr/Y	0.6	0.5	0.5	4.1	3	2.2	1.4	3.7	2	3.9	4.6	1.4	0.8
ΣРЗЭ	160	182	227	166	229	199	92	78	96	107	116	124	85

prismatic crystals more often with simple twins, less often with polysynthetic twins; sometimes form glomerular coalescence. The alkaline feldspar phenocrysts are slightly sericitized and sometimes replaced by hydromuscovite on micro-cracks. The groundmass of quartz-feldspar sometimes recrystallized. Rare small flakes of chloritized biotite with rutile inclusions along cleavages are observed. The ore minerals are magnetite and titanomagnetite; and in subordinate – by leucoxene. Xenocrysts are absent.

The R2-rhyolite easily diagnosed due to the light colors and aphyric or aplite-like appearance (Fig. 5f–g). Relict porphyritic texture is observed. Phenocrysts (1–3%) are represented by semi-decomposed prismatic crystals of alkaline feldspar (0.4–0.7 mm), with inclusions of micro-lamellae rutile and leucoxene, and alteration of clay minerals such as kaolinite. The groundmass is made of secondary-spherulitic quartz-feldspar aggregates, black dusty particles of leucoxene (up to 1–3%), and yellowish-brown kaolinite.

The R3-rhyolite is more alterated than the other types. They have a light yellowish colors, and glomeroporphyritic textures (Fig. 5h, i). The rock is massive and heterogeneous, taxitic, flow-banded, festoon-fluidized. Phenocrysts (from 0.2 to 2.5 mm), in an amount of 10–20% of the rock volume are represented by quartz and feldspar. Quartz forms isometric less often comminuted grains with melted edges. The feldspar phenocrysts are intensively exposed to secondary processes. Etching shows spotted K-feldspathization at the periphery and along the micro-cracks, often in the form of solid microcline lattice or in a staggered manner on the central part. There is a germination of small differently oriented prisms of albite. Felsitic texture in combination with micro-poikiloblastic, relict- and secondary-spherulitic textures are dominated. These rocks are characterized by wide development of chloritized biotite flakes with rutile secretions along cleavage. Secondary alterations are expressed in K-feldspatization, silicification, spotted-banded sericitization, weak chloritization. In some cases, there are magmatic breccias of rhyolites, resembling automagmatic breccias. Captured material is represented by rhyolites xenoliths and xenocrysts of quartz and feldspars (0.25–0.75 mm).

5.2. Zircon U-Pb geochronology

U-Pb dating of zircons from samples of the R1-rhyolites (MS-26, MS-10/1, MS-8, MS-12, MS-14/1), R2-rhyolites (MS-13/1), and R3-rhyolites (MS-32) provided time constraints on the emplacement of the subvolcanic intrusions of the Melnichno-Sosnovsky volcanic complexes in the NW Rudny Altai. The $^{206}Pb/^{238}U$ ages of the R1-rhyolite were obtained for six samples of main phase of the Voronezh, Karaulny, Butochny, Sadovushka and Kruchki volcanic centers. The zircon grains of sample №MS-26 (Voronezh) are colorless or pale yellow euhedral prismatic crystals (80–350 μm, $KL = 2–3$), with oscillatory zoning in CL-images, indicating magmatic origin (Fig. 6a). A weighted mean $^{206}Pb/^{238}U$ age of 388 ± 2 Ma (MSWD = 0.12) was obtained for 37 analytical spots in different parts of zoned magmatic crystals (Nos. 1–37 in Table 1) and interpreted as the age of emplacement (Fig. 6f). The zircons of №MS-10/1 (Karaulny) are transparent, translucent, colorless, pale yellow and pale brown euhedral prismatic crystals (150–270 μm, $KL = 2–2.5$) with thin oscillatory zoning (Fig. 6b). A weighted mean $^{206}Pb/^{238}U$ age of 389 ± 3 Ma (MSWD = 0.06) was obtained for 12 analytical spots in different parts of zoned magmatic crystals (Nos. 17–28 in Table 1) and interpreted as the age of emplacement (Fig. 6g). However, 16 analyses for the same sample (Nos. 1–16; Table 1) gave weighted mean $^{206}Pb/^{238}U$ age of 381 ± 2 Ma (MSWD = 0.44). Since these rhyolites are the same as R1-samples; and the zircons from this sample were separated in one batch with the zircons from R2-rhyolite, we assume that clogging of this sample could occur. If we calculate the total weighted average age obtained for all zircon grains from this sample, it yields a value of ~384 Ma, which contradicts the stratigraphic data, since at this point there was a volcanic pause in the NW Rudny Altai (Fig. 3; Murzin et al., 2001). On the other hand, the

obtained variations of $^{206}Pb/^{238}U$ isotopic ages are still within the accuracy of the LA-ICP-MS method used. Zircon grains of sample №MS-8 (Butochny) are euhedral prismatic crystals (70–120 μm, *KL* = 1.5–2.0), translucent, colorless or pale yellow. CL-images reveal thin oscillatory magmatic zoning (Fig. 6c). The weighted mean $^{206}Pb/^{238}U$ age for 17 analyses (Nos. 1–13; Table 1; Fig. 6h) is 389 ± 3 Ma (MSWD = 0.4). The zircon grains of sample №MS-12 (Sadovushka) are translucent colorless or with a yellowish tint euhedral prismatic crystals (70–110 μm, *KL* = 1.5–2), with oscillatory zoning in CL-images (Fig. 6d). Fifteen analyses yield a weighted mean $^{206}Pb/^{238}U$ age of 389 Ma (MSWD = 0.01) for different parts of zoned magmatic crystals (Nos. 1–5; Table 1) and interpreted as the age of emplacement (Fig. 6i). The zircon grains of sample №MS-14/1 (Kruchki) are colorless or pale yellow euhedral prismatic crystals (70–200 μm, *KL* = 1.5–4), with oscillatory zoning in CL-images (Fig. 6e). A twelve sub-concordant analyses yield a weighted mean $^{206}Pb/^{238}U$ age of 391 Ma (MSWD = 0.03) for different parts of zoned magmatic crystals (Nos. 1–12; Table 1) and interpreted as the age of emplacement (Fig. 6j). The zircon grains of sample №MS-13/1 (Sadovushka) are transparent-translucent, colorless or slightly yellowish euhedral prismatic and isometric crystals (90–200 μm, *KL* = 2–3), with oscillatory zoning in CL-images (Fig. 7a). A weighted mean $^{206}Pb/^{238}U$ age of 381 Ma (MSWD = 0.86) was obtained for 13 analytical spots in different parts of zoned magmatic crystals (Nos. 1–13; Table 1) and interpreted as the age of emplacement (Fig. 7c). Additional 3 analyses gave a weighted mean $^{206}Pb/^{238}U$ age of 422 Ma (MSWD = 0.49) interpreted to record the age of inherited zircons (Nos. 14–16; Table 1).

The zircon grains of sample №MS-32 (Butochny) are translucent colorless or slightly yellowish euhedral prismatic and isometric crystals (80–170 μm, *KL* = 2–4), with oscillatory zoning in cathodoluminescence (CL) images (Fig. 7b). A weighted mean $^{206}Pb/^{238}U$ age of 381 Ma (MSWD = 2.2) was obtained for 6 analytical spots in different parts of zoned magmatic crystals (Nos. 1–6; Table 1) and interpreted as the age of emplacement (Fig. 7d). Thirteen additional analyses gave a weighted mean $^{206}Pb/^{238}U$ age of 404 Ma (MSWD = 0.09), which may record the age of xenocrytic or inherited zircons (Nos. 7–19; Table 1).

5.3. Mobile element geochemical systematic

Twenty-eight samples of rhyolites have been analyzed for major- and trace-element abundances and results are listed in Table 2. Loss on ignition mostly ranged from 0.2 to 2% and the major elements compositions have been recalculated on an anhydrous basis to 100 wt%. Although rhyolite samples were taken away from the ore bodies to avoid the possible effect of secondary mineralization, the rhyolites still show chemical vagaries due to feldspathization (enrichment in soda or potash) and silicification (enrichment in silica).

Most of the MS-rhyolites have very high contents of SiO_2 (75.5–79.4 wt%), low Al_2O_3 (8.3–12.5 wt%) and very low CaO (0.05–1.35 wt%) and MgO (0.01–0.9 wt%). These rocks have a wide variation in the amount of $Na_2O + K_2O$ (2.7–9.3 wt%), and formally have affinity to sub-alkaline series, in the TAS diagram (Fig. 8a; Le Maitre et al., 1989); and to low-K tholeiite and medium-K calc-alkali series, in the SiO_2-K_2O diagram (Fig. 8b; Peccerillo and Taylor, 1976). This determines their division into two groups: most R1 (n = 15) and R2-rhyolites (n = 2) have a weak predominance of sodium over potassium (Na_2O = 2.6–4.8 wt%; K_2O = 0.1–4.3 wt%); and in contrast, all R3-rhyolites (n = 6) and some samples from the first group have a predominance of potassium over sodium (Na_2O = 0.1–2.6 wt%; K_2O = 4.1–8.6 wt%). In addition, these rock have a predominantly high Fe^* Index ($Fe^* = FeO^T/(FeO^T + MgO)$; Frost et al., 2001; Fig. 8c) from 0.88 to 1.00 (n = 15); and extremely strongly peraluminous values of the Aluminum Saturation Index from 1.2 to 5.6 (*ASI* = Al/(Ca–1.67P + Na + K) molar ratio; Chappell and White, 1992; Fig. 8d).

In fact, MS-rhyolites consist of relatively immobile Si and Al, which do not vary greatly in amount, and mobile K and Na components, which have wide variations (Table. 3). Some strongly altareted rhyolites have extremely felsic composition (SiO_2 = 84.9–86.3 wt%) or extremely strongly contrast Na_2O/K_2O (0.02 to 39.6 wt%) ratios. From the entire rocks, only three R1-samples (ms-10/1; 14/2 and 14/3) have the lowest SiO_2 ~ 76 wt% and alkalis from 6.2 to 7.8 wt%, which are probably the closest reflection of the primary composition of these rocks. In term of major elements, this causes difficulties and can give confusing conclusions on the classification of such high-siliceous rocks, with sodium/potash dichotomy; given also the absence of less felsic varieties with which they could form a single series suitable for analysis and identification.

5.4. Alteration effect

The mobile-element variations in the volcanic rocks of submarine environment are a result of spilite-keratophyric alteration – mass exchange components due to active fluid-magma/rock interactions, due to magma reaction with down-welling cold sea water and/or outflowing hot hydrothermal fluids. Essentially this is the result of chloritization (Mg-Fe alterations), and albitization (Na-K exchange reactions) – dramatic increase in normal albite balance in hydrolysis of feldspar, accompanies by relatively addition or removal of silica and alumina (Alt and Teagle, 2003). In previous works, it was noted that (i) the felsic effusive of the Rudny Altai are not a particular type of ultra-felsic and ultra-sodium rocks, but were subject to intense secondary alteration pronounced in silicification and albitization; and (ii) although the volcanic rocks of the Rudny Altai were formed in submarine conditions, albitization was subject not only to effusions, but also to Devonian granites, which excludes the major role of sea water in this process (Chernov, 1974). Thus, subvolcanic intrusions with MS-rhyolites probably could not interact directly with seawater.

Based on our data, only R1-rhyolite could be effected to some sodium enrichment by fluid-related alterations, as evidenced by the positive correlation between Na and LOI, and *ASI* Index, and the high values of this index in samples with high Na contents (Fig. 9a). In contrast, for high-K R3-rhyolite, there is not relationship between *ASI* Index and Na, and between LOI and Na, suggesting that they are free of sodium fluid-related alterations. On the one hand, the “Igneous Spectrum” diagram (Hughes, 1972), reflecting K/Na variations in spilite-keratophyric rocks, the R1-rhyolite plot in the field of weakly altered rocks; while all R3- and some of R2-rhyolites are in the field of compositions modified by potassic metasomatism (Fig. 9b). Also it corresponds to discrimination of compositions on the “Alteration Box Plot” diagram (Fig. 9c; Large et al., 2001), reflecting the geochemical trends of diagenetic and hydrothermal alterations in the rocks, which shows most R1- and R2-rhyolites are in the field of least altered rhyolites; and, in contrast, the R3-rhyolites are the boundary between diagenetic and hydrothermal alterations fields. On the other hand, for R3-rhyolites there is no direct relationship between K_2O and LOI; and LOI values are not the highest (Fig. 9a; Table. 2). This suggests a lack of relationships between the high K_2O contents in these rocks and any potash enrichments, associated with exposure to hydrothermal fluid on the solid rock. Our analysis shows that the strongly altered rocks from are only six samples of R1- and R2-rhyolites, with the highest SiO_2 contents and extreme Na/K ratios (Table. 2). On the “Alteration-Box-Plot” diagram, they lie outside the last change of least altered rhyolitic field and show a clear dichotomy of compositions into soda- and potash-rich varieties (Fig. 9c). Clearly, the wide variations in the petrochemical compositions of strongly altered rocks are not a primary igneous feature, but instead are a result of intense secondary alteration that occurred most likely at the post-magmatic stage.

The effects of alkaline-fluid alterations are also shown by variations of some other major and trace elements. Of course, the fluid-mobile elements (e.g. Ba, Rb, Cs and Sr) concentrations could be strongly modified in the increasing degree of feldspathization process because they

Table 3
Sm-Nd isotopic compositions for representative samples of the MS-rhyolite.

Sample	Volcanic center	Type	Sm	Nd	$^{147}Sm/^{144}Nd$	$^{143}Nd/^{144}Nd$	Err (2σ)	$E_{(Nd)}0$	$E_{(Nd)}$-t	T_{DM} (Ma)	T_{DM2} (Ma)
ms-26	Voronezh	I	5,27	26,75	0,119,157	0,512,504	9	−2,61	1,25	1044	1050
ms-10/1	Karaulny	I	11,63	53,1	0,130,190	0,512,622	7	−0,31	3,01	966	903
ms-8	Butochny	I	6,52	29,2	0,134,932	0,512,648	14	0,20	3,28	974	880
ms-12	Sadovushka	I	4,61	20,59	0,135,373	0,512,701	20	1,23	4,29	877	795
ms-14/2	Kruchki	I	7,52	31,27	0,145,409	0,512,700	16	1,21	3,70	1008	838
ms-32	Butochny	III	3,68	14,86	0,149,607	0,512,449	9	−3,69	−1,41	1669	1263

replace Na, K, and Ca, due to their mobility during hydrothermal alternation and metamorphism (Ayers et al., 2012; Wilke et al., 2012). For example, Rb/Sr ratios for most MS-rhyolites are very low from 0.05 to 0.9, reaching ~4.5 in only three samples. However, as indicated by variation of the Na and K, for weakly altered samples the values of elements such as Al, Ti, Ga, Ga/Al, and Zn are probably modified only marginally. For this study, it is relevant that the aqueous solubility of Zr may increase with the addition of Na-Al-Si-bearing hydrothermal fluids, and it can play an important role for mobilization of HFSEs and change of the isotopic system during fluid-rock interaction (Ayers et al., 2012; Wilke et al., 2012). Although most of the R1- and R3-rhyolites have wide variations of Na/Al ratios reflecting relatively modification of the compositions by alkaline fluid, nevertheless they are observed in a narrow range of Zr contents, which do not have a clear correlation with Na/Al ratios (Fig. 9d). The exception is the four strongly altered potash-rich R1-samples on the left side of this diagram, which have low Na/Al ratios correlating with Zr values.

The rare earth elements (REE), and even more so Eu, could also be mobile during intense hydrothermal or low-grade metamorphic alteration; and light REE (LREE) are considered to be more susceptible to mobility than heavy REE (HREE) under most conditions (Polat and Hofmann, 2003). However, as shown by Fig. 9e, for weakly altered R1-

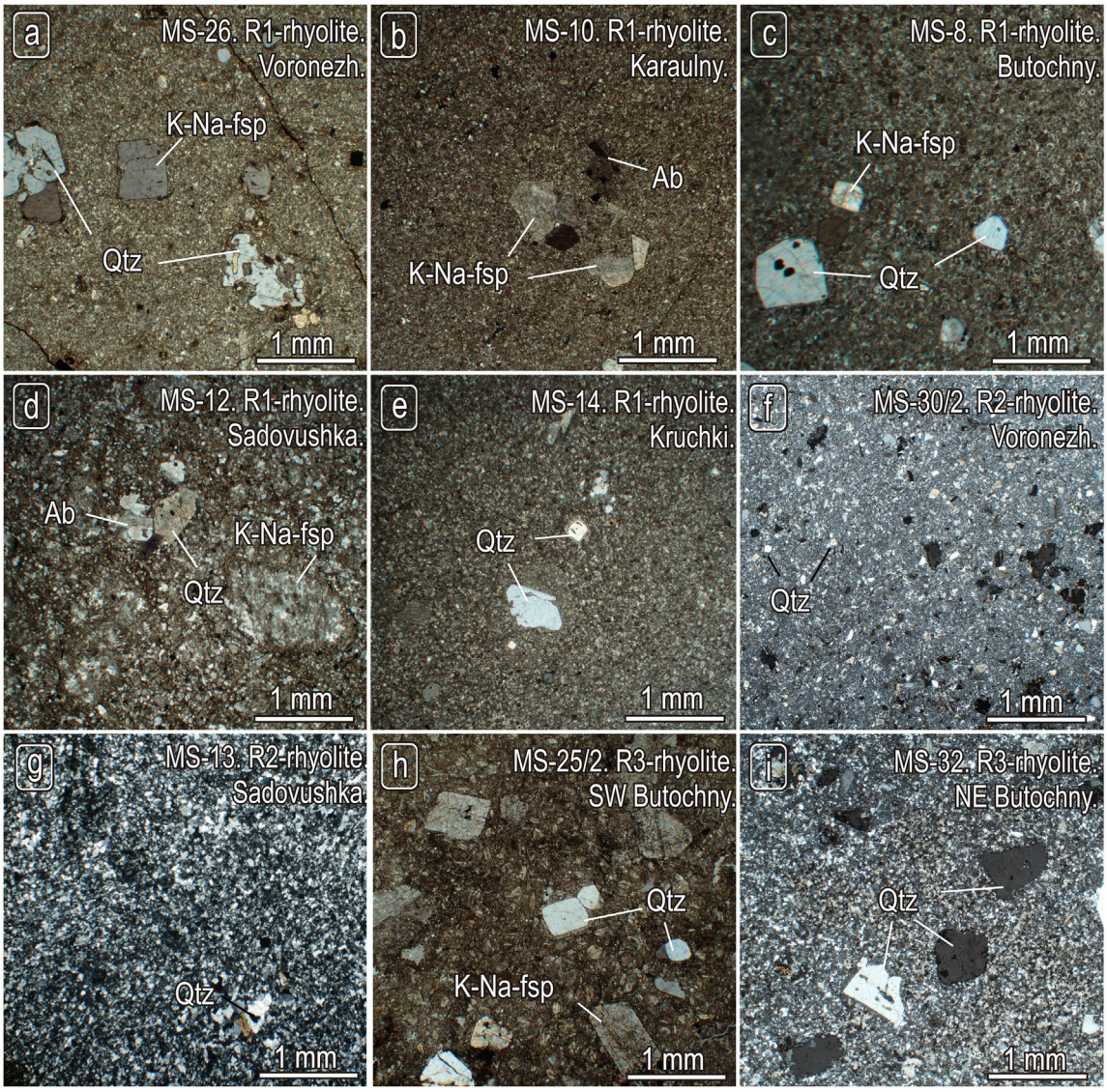

Fig. 5. Micro-photos of representative rhyolite samples. R1-rhyolite (a–e); R2-rhyolite (f–h); and R3-rhyolite (i–l). Pl = plagioclase, Kfsp = K-feldspar, Qtz = quartz, Bt = biotite. For details of data selection see Section 5.1.

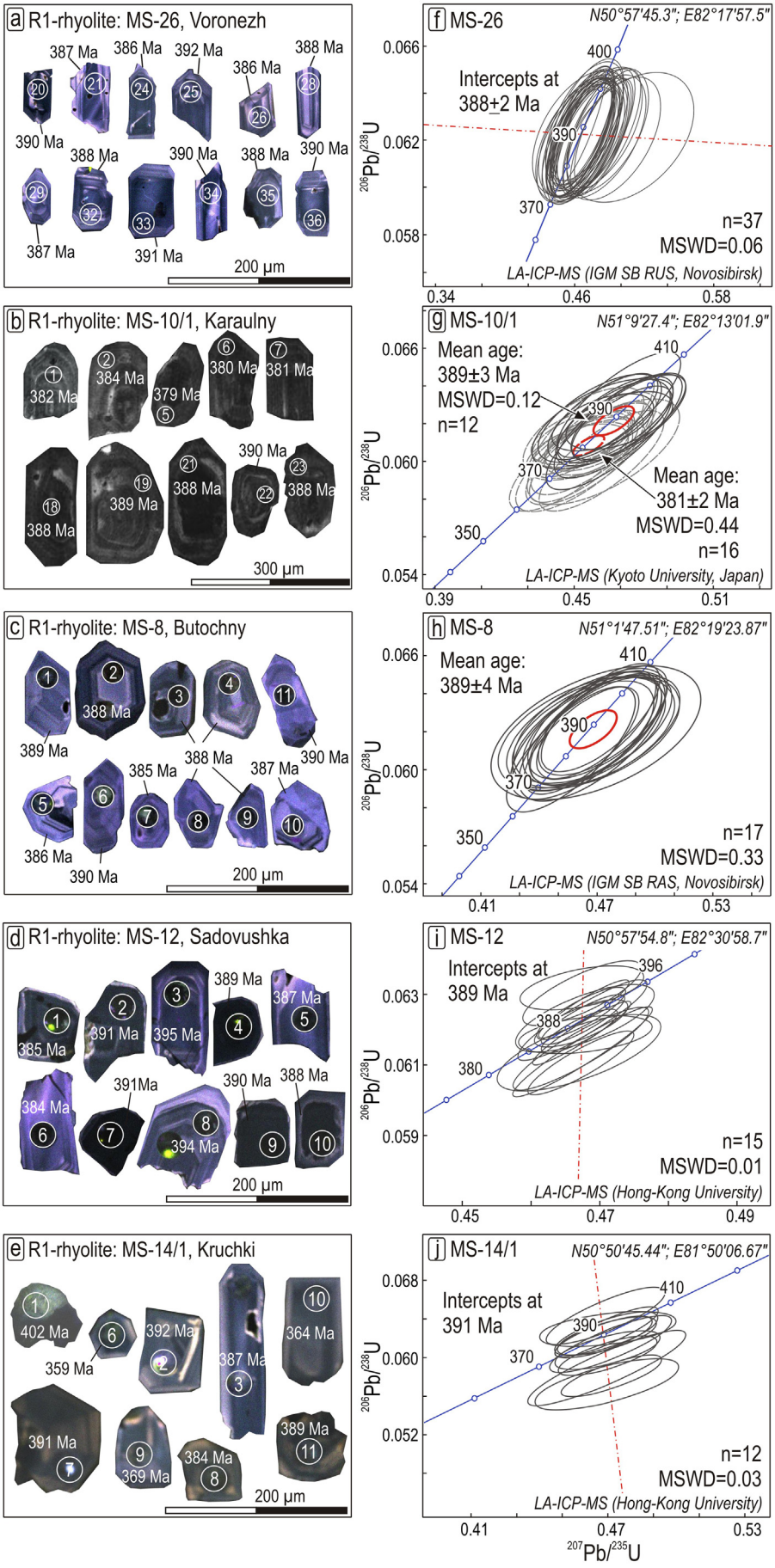
a R1-rhyolite: MS-26, Voronezh
387 Ma
386 Ma
392 Ma
388 Ma
386 Ma
390 Ma
388 Ma
390 Ma
388 Ma
390 Ma
387 Ma
391 Ma
200 μm
b R1-rhyolite: MS-10/1, Karaulny
382 Ma
384 Ma
379 Ma
380 Ma
381 Ma
388 Ma
389 Ma
390 Ma
388 Ma
388 Ma
300 μm
c R1-rhyolite: MS-8, Butochny
389 Ma
388 Ma
385 Ma
388 Ma
387 Ma
390 Ma
386 Ma
390 Ma
200 μm
d R1-rhyolite: MS-12, Sadovushka
385 Ma
391 Ma
395 Ma
389 Ma
387 Ma
384 Ma
391Ma
394 Ma
390 Ma
388 Ma
200 μm
e R1-rhyolite: MS-14/1, Kruchki
402 Ma
359 Ma
392 Ma
387 Ma
364 Ma
391 Ma
369 Ma
384 Ma
389 Ma
200 μm
f MS-26
N50°57'45.3"; E82°17'57.5"
Intercepts at
388±2 Ma
n=37
MSWD=0.06
LA-ICP-MS (IGM SB RUS, Novosibirsk)
g MS-10/1
N51°9'27.4"; E82°13'01.9"
Mean age:
389±3 Ma
MSWD=0.12
n=12
Mean age:
381±2 Ma
MSWD=0.44
n=16
LA-ICP-MS (Kyoto University, Japan)
h MS-8
N51°1'47.51"; E82°19'23.87"
Mean age:
389±4 Ma
n=17
MSWD=0.33
LA-ICP-MS (IGM SB RAS, Novosibirsk)
i MS-12
N50°57'54.8"; E82°30'58.7"
Intercepts at
389 Ma
n=15
MSWD=0.01
LA-ICP-MS (Hong-Kong University)
j MS-14/1
N50°50'45.44"; E81°50'06.67"
Intercepts at
391 Ma
n=12
MSWD=0.03
LA-ICP-MS (Hong-Kong University)
206Pb/238U
207Pb/235U

rhyolites, there is no correlation between La/Sm and Gd/Yb ratios, and the values of "Alteration Index" (*AI*; Lentz, 1998). In addition, the REEs (Fig. 9f) and HFSEs (Fig. 10) for all R1-rhyolite show linear trends with Zr contents, and as shown below, there is a coherent character of chondrite-normalized REE-patterns, attesting to their relative immobility. As for R3-rhyolites, our analysis clearly shows that wide variations of La/Sm ratios in these rocks were clearly not related to either feldspathization or chloritization, as their compositions form a subvertical trend on the La/Sm vs *AI* diagram (Fig. 9e). There is no clear correlation between Zr and REEs; but their compositions are not scattered randomly on the diagram, as if they were secondary modified. The observed distribution of compositions most closely resembles the magmatic trend of differentiation. In general, we suggest that for most MS-rhyolites their REEs and HFSEs were relative immobile during hydrothermal alterations, and we thus use these elements to identify the original geochemical type of these rocks.

5.5. Immobile element geochemical systematics

Firstly, on the Nb/Y-Zr/TiO_2 diagram (Winchester and Floyd, 1977), rocks of this study demonstrate affinity to a "normal-type" rhyolite, although several samples are on the border of the field comendite/pantellerite (Fig. 10a). When incompatible elements, such as REEs, Zr, and Y are used, the MS-rhyolites are characterized by transitional compositions between calc-alkaline and tholeiitic series: $(La/Yb)_n$ ~ 3–6 (Fig. 10b; Lentz, 1998; C1 chondrite values of Sun and McDonough, 1989); and Zr/Y ~ 4 при Zr < 350 ppm (Fig. 10c); and La/Sm ~ 0.55–1 (Fig. 10d; Lentz, 1998; Barrett and MacLean, 1999). On the discrimination diagram of La/10-Y/15-Nb/8 (Cabanis and Lecolle, 1989), the R1-rhyolite is marked on the boundary between the field of the arc-related calk-alkaline series and the within-plate series; and R2- and R3-rhyolites have a geochemical affinity with the within-plate series (Fig. 11).

The relationships between Nb, Y, Zr and Ce, and ratios of Ga/Al (1.26–3.52), and Zn (9–187 ppm) concentrations, show that the R1-rhyolite has continuous transitional characteristics between the *OGT* (unfractionated *M*-, *I*- and *S*-granite) and *A*-type felsic rocks (Fig. 12a-f; Whalen et al., 1987). In contrast, the R2- and R3-rhyolites are marked only in the *OGT*-field, since the total Nb, Y, Zr and Ce (119–242 ppm), and Ga/Al (0.51–1.39) values; and Zn (52–171 ppm) contents are relatively low. In the Nb vs. Y and Rb vs. Y + Nb tectonic discrimination diagrams (Pearce et al., 1984), all of the rhyolites are transition between volcanic-arc (*I*-type) and within-plate (*A*-type) fields (Fig. 12g-h; Whalen et al., 1987). Although the variations in Rb are coherent with K_2O, we neglected it in this case because the reason for that the rhyolites compositions plot on the border between the fields of normal arc-related and within-plate felsic magmas is due to Y + Nb (32–92 ppm) and Ta + Nb (7–15 ppm) abundances. All rhyolites possess low Rb (<200 ppm) contents, which is incompatible with a syn-collision setting (Fig. 12h). Consequently, some of the R1-rhyolite bear the distinctive geochemical signature of *A*-type felsic magmas, such as: (i) total enrichment in Zr, Nb, Y and Ce (>350 ppm), Zr (>250 ppm), and high Ga/Al values (>2.6; Whalen et al., 1987). In general, if we consider all MS-rhyolites, they have transitional geochemical characteristics that resemble those of felsic rocks of the subduction-related extension geodynamic settings. However, this magmatism was unlikely to be associated with the rebound of the oceanic plate following slab break-off and extensional detachment of subduction orogen, like the Cordillera of North America (Whalen and Hildebrand, 2019); Fig. 12j.

Secondary, analysis of geochemical patterns shows that all rhyolites can be divided into two groups, which corresponds to the main and late phases of magmatic activities. The difference in REEs concentration and the degree of Eu anomaly are distinctive feature of these rhyolites (Fig. 13). One group (R1-rhyolite) has higher REEs (104–260 ppm) concentration, generally show coherent spectra with more fractionated REEs ($(La/Yb)_n$ = 1.57–6.69), nearly flat to positive HREEs patterns ($(Gd/Yb)_n$ = 0.81–1.71), and moderate negative Eu anomalies (Eu/Eu^* = 0.35–0.76; $Eu^* = 2Eu_n/(Sm_n + Gd_n)$), in the chondrite-normalized REEs diagrams (Fig. 13a; C1 chondrite values of Sun and McDonough, 1989). In contrast, another group (R2- and R3-rhyolites) has relative low REEs concentration (78–124), less fractionated REEs ($(La/Yb)_n$ = 2.95–5.82), and nearly flat to negative HREEs patterns ($(Gd/Yb)_n$ = 0.38–1.52), along with a pronounced negative Eu anomaly (Eu/Eu^* = 0.18–0.4); Fig. 13c. For all of the rhyolites, the N-MORB-normalized multi-element patterns (Sun and McDonough, 1989) are characterized by sub-parallel spectra and homogeneous with prominent and uniform enrichment in Rb, Ba, Th, U and negative anomalies in Nb, Ta and Sr, and with slight to moderate variations in element abundances. In general, the rhyolites of the first group are more enriched in Zr, Hf, and Zn, Ni and V, and the rhyolites of the second group are enriched in Rb, Ba and Pb, Cr, although these regularities are not systematic. As noted in many works, some of the geochemical signatures, such as depletion in HFSEs: Nb, Ta and Ti relative to LILEs and LREEs, it is a common feature of felsic magmas formed in convergent margin settings, and derived from a crystal source, which itself was derived from arc crust (e.g. Whalen et al., 1996).

Thirdly, although we have summarized the geochemical characteristics of MS rhyolites, their initial geochemical type is still difficult to identify. As suggested to us Prof. Bruno Scaillet "All the types discussed here are metaluminous". (i) Obviously, the parental magmas of the MS-rhyolites were hardly peralkaline in nature, as was observed from their Zr/Ti and Nb/Y ratios (Fig. 10a and Fig. 12j). (ii) It is also unlikely that these magmas were peraluminous type, because they have *A*-type evolutionary trend (Fig. 12f), and are clearly different from highly fractionated *S*- and *I*-type granites, that would increase their Ga/Al ratios при crystal differentiation (Wu et al., 2017). (iii) As discussed below, the R2- and R3-rhyolites are somewhat resemble high-silica residual and non-equilibrium melts associated with *A*-type magmas (Barboni and Bussy, 2013); Fig. 12f. In general, this indicates that the parental magmas of the MS-rhyolites should have been metaluminous.

Fourth, in comparison with the bimodal-type extensional rhyolites of different subduction-related environments (Fig. 13a), the R1-rhyolites REE-patterns have a close resemblance to those of felsic volcanic rocks of intra-oceanic back-arc basin, as shown by the example of the Izu-Bonin convergent system (Tamura et al., 2009). They show even greater geochemical affinity to the extensional rhyolites of the bimodal association of the Coastal Range in the Central Chile, related to Late Triassic intra-continental rifting in the Pacific Gondvana margin (Fig. 13b; Morata et al., 2000). There is also a geochemical similarity to some of the bimodal-type rhyolites of Taupo Volcanic Zone, New Zealand (Deering et al., 2011), although the latter are mostly characterized by more depleted concentrations of MREEs and HREEs (Fig. 13b). As for the R2- and R3-rhyolites, it have the so-called seagull-like form of REE-patterns, which, in the simplifying assumptions, resemble those of some fractionated granites (*FG*) and A_2-type granites attributed to post-orogenic extension tectonic setting (Chappell and White, 1992; King et al., 1997; Chappell, 1999). However, all of the MS-rhyolites are clearly distinguished from post-orogenic granites, by a general depletion in REEs, lower HFSEs (e.g. Nb ~ 7–13 ppm; Th ~ 5–10 ppm) contents, and less pronounced Eu anomaly (Fig. 12c, d), for example, if we compare them with A_2-granite from Southern Altai Range, China (Shen et al., 2011). By the same geochemical characteristics, they differ from bimodal-type rhyolites associated with initial rifting, as in Miocen ridge-subduction-related California-type environments (Johnson and O'Neil, 1984; Cole and Basu, 1992). Compared to R2- and R3-rhyolites, some bimodal-type rhyolites from Eastern Tianshan Belt in Northwest China (Chen et al., 2011) have a similar form of REE-patterns, reported

Fig. 6. (a–e) Representative cathodoluminescence images (CL) of zircons of R1-rhyolites. (f–j) U-Pb dating results and concordia diagrams for the selected ages. For details of data selection see Section 5.2.

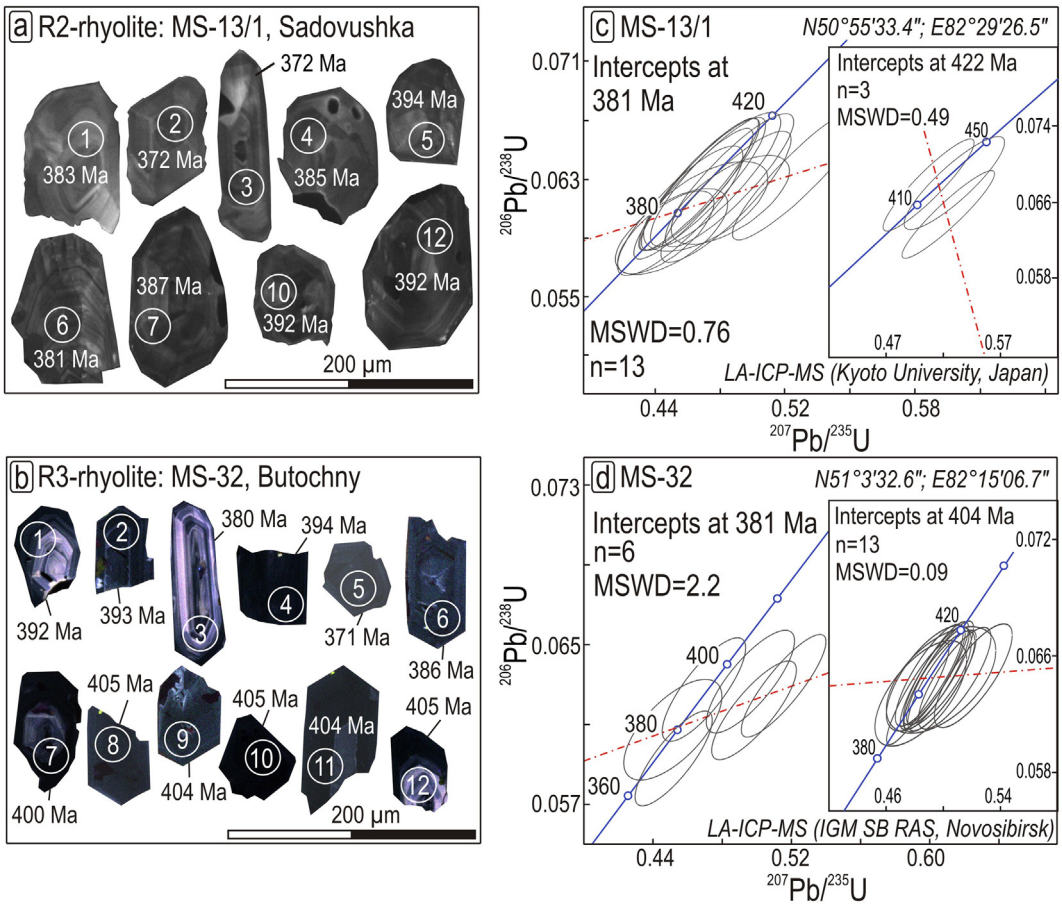

Fig. 7. (a, b) Representative CL-images of zircons of R2- and R3-rhyolites, respectively. (c, d) U-Pb dating results and concordia diagrams for the selected ages. For details of data selection see Section 5.2.

for the initial post-orogenic rifting settings (Fig. 13d); and Okinawa Through rhyolites are associated with rifted-arc Ruykuy (Shinjo and Kato, 2000); and Kuroko Rift rhyolites are associated with volcanic activity in the NE Honshu back-arc system (Yamada et al., 2012). Our analysis shows that there is some regularity in the affinity of REEs characteristics of MS-rhyolites with those of the bimodal-type rhyolites related with the modes of extension of the continental type of the lithosphere, as in mature/marginal island-arc and continental margin, and in some post-collisional settings.

5.6. Isotopes

Most of the MS-rhyolites have elevated values of $^{143}Sm/^{144}Nd$ ~ 0.13–0.14, compared to values for the average continental crust (~0.12; Liew and Hofmann, 1998); and $\varepsilon Nd(t)$ from +3.0 to +4.3, and model ages of $T_{Nd}(DM\text{-}2)$ ~ 0.79–0.9 Ga (Fig. 14; Table. 3). Coherent normalized REE patterns and lack of correlation with the variations of Na/Al (inset to Fig. 14), indicate that secondary alteration have not significantly changed their Nd isotopic composition. The exception is the strongly altered rhyolite №MS-26 (Tables 2, 3), which has values $\varepsilon Nd(t) = +1.25$ and model age of $T_{Nd}(DM\text{-}2) = 1.05$ Ga. Since this sample has very low Na/Al values, the modification of its isotopic composition was probably due to post-magmatic potassium metasomatic alterations.

6. Discussion

6.1. Rocks source

Firstly, it is suggested that the main sources producing felsic magmas of bimodal association in the subduction-related extensional environments may be: (i) amphibolitic crust of ancient basement, such as the Pacific convergent margin of the North American plate (Piercey et al., 2008); (ii) newly formed basalt-andesitic crust, as for example, from Izu-Bonin intra-oceanic subduction system (Tamura et al., 2009); or (iii) the greywackes or previously emplaced igneous rocks, like in Taupo Volcanic Zone, New Zealand (e.g. Deering et al., 2011). In term of the experimental constraints on the formation of silicic magmas (see review in Scaillet et al. (2016)), metaluminous melts are typically originated from igneous sources, either via fractional crystallization of mafic magmas or by partial melting of older, crustal metaluminous intrusive during which biotite and amphibole breakdown takes place. The absence of adakites signature (e.g. Sr/Y < 40 and Yb > 1.8 ppm; Xiao and Clemens, 2007) in the MS-rhyolites suggests that their parent magma was not in equilibrium with a garnet-bearing residue. During partial melting, garnet is not stable in residue under pressures below 8 kbar for tonalitic (Rutter and Wyllie, 1988; Watkins et al., 2007) and 6 kbar for volcanoclastic (Castro et al., 2000) sources.

Secondary, it may seem that the moderate isotope signatures (εNd (t) from 3.0 to 4.3; Table 3; Fig. 14) and relatively young Nd model ages (mostly 0.8–0.9 Ga) of the MS-rhyolite indicate possible presence of mixed mantle and crustal components, for example, mixing/mingling of mafic and felsic magmas caused by basaltic underplating (Wilson et al., 2005). However, the stratigraphic position of the mafic volcanogenic-sedimentary rocks filling the Shipunikha rift clearly indicates their generation after the formation of subvolcanic intrusions of MS-rhyolites (Murzin et al., 2001). Thus, the partial melting of underplating new mafic crust, in the form of known Devonian basic rocks, could not play an important role. In addition, trend of the zircon-saturated crystallization for the MS-rhyolites differs from the trend of high-*T I*-type felsic magmas produced by the partial melting of mafic

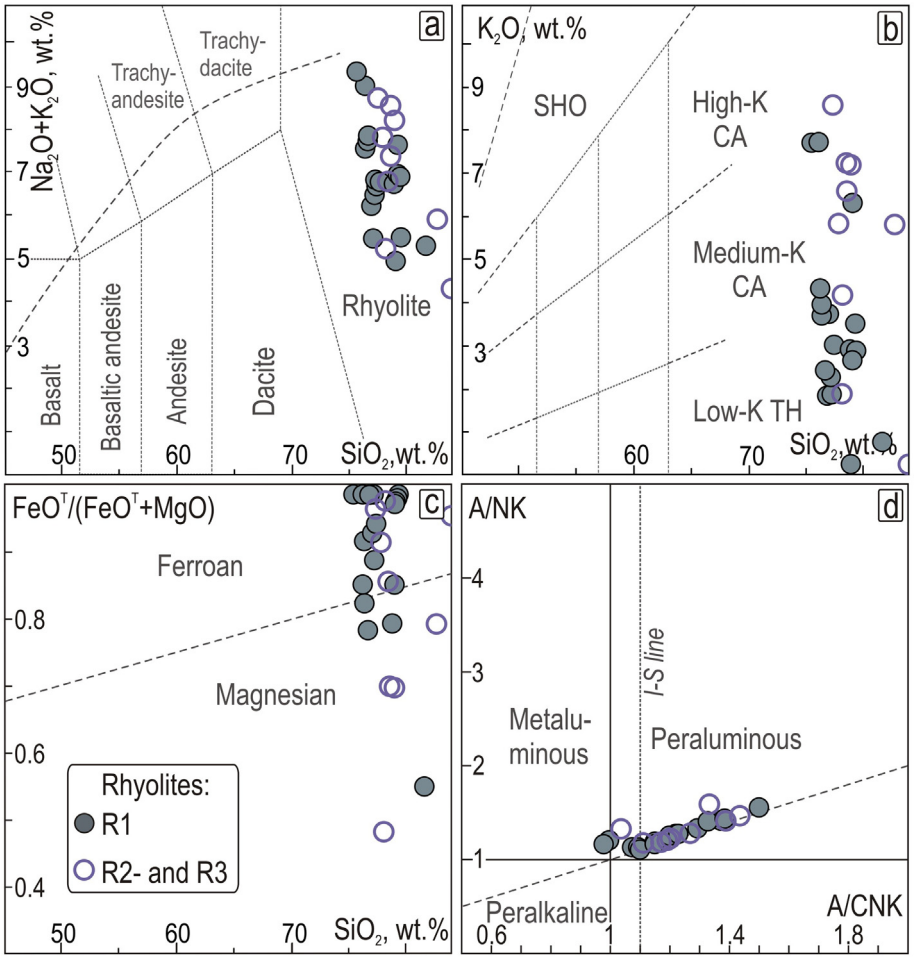

Fig. 8. Major element classification of the MS-rhyolites. (a) Total alkalis vs. Silica diagram (Irvine and Baragar, 1971; Le Maitre et al., 1989), division according to (Middlemost, 1994). (b) K_2O vs. SiO_2 alkalinity diagram (Rickwood, 1989). (c) $FeO^T/(FeO^T + MgO)$ vs. SiO_2 (wt%) diagram (Frost et al., 2001). (d) Aluminum Saturation Index (Al/(Ca-1.67P + Na + K vs. Al/(Na + K) molar ratio)) diagram (Shand, 1943). The diagrams show the extreme petrochemical characteristics of the MS-rhyolites.

metaigneous source (Fig. 16a; King et al., 1997); and MS-rhyolites are clearly enriched in LREEs with respect to metabasalt-derived felsic magmas when compared to intra-oceanic arc-related bimodal-type rhyolites (Fig. 13a; Tamura et al., 2009). Note also that in addition to hybrid isotope values in the MS-rhyolite, and later tuffs of mixed composition, there is no clear geological evidence of mantle-crust interaction in the Rudny Altai. We suggest that the isotope compositions for the rhyolites could be related to the involvement of immature sediments in their petrogenesis, which have juvenile isotopic compositions. Volcanoclastic and continental detritus sediments were widespread along the continental margin, which consists of biotite, amphibole, plagioclase, and quartz and may have been brought to the magma sources of granitoids (Vielzeuf et al., 1990). Fig. 14 shows that the isotopic composition of MS-rhyolites are closest to the field of evolution of Nd isotopic composition for the Early Devonian (our data) and Caledonian volcanic rocks (Kruk et al., 2010; Kruk, 2015), which, in the form of clastic material, could be transported from the Altai Mountains (Hu et al., 2000), and sedimented on the continental shelf prior to Devonian volcanism.

6.2. Zircon saturation

The R1-rhyolite is characterized by enrichment in Zr (109–378 ppm), and there are no inherited zircon crystals (see Section 6). The high Zr content is more likely to suggest partial melting of the upper crustal materials (Zr ~ 160–240 ppm; Rudnick and Gao, 2003), than formation due to mantle-related source. As discussed above, the MS-rhyolites belong to the "normal" type felsic volcanic rocks. This means that the enrichment in Zr does not come from the peralkaline nature of their magmas (Scaillet et al., 2016). We suggested, that the absence of ancient zircons is indirectly confirmed the high zircon saturation temperatures (Watson and Harrison, 1983; Clemens et al., 1986; Eby, 1990; Boehnke et al., 2013). At dissolution of accessory phases during the melting processes, melts gain heat producing and incompatible elements is facilitated in *A*-type granitic magmas because they are high in temperature and largely molten (King et al., 1997). For example, Zr vs. SiO_2 variation diagrams (Fig. 16a) shows that Zr in the R1-rhyolites decrease toward more felsic compositions, similar to the trends in *A*-types felsic magmas derived from a quartz-feldspathic source with Zr-saturation (King et al., 1997). In addition, it is empirically established that *A*-type felsic rocks have 2 to 3 times higher Zn contents, than compositionally similar *S*-, *I*-, and *M*-types granitoids and related volcanic rocks (<60 ppm), because of the high solubility of Zn at high temperature in such magmatic systems (Fig. 16b; Lentz, 1998). The R2- and R3-rhyolite have low Zr concentrations (53 to 78 ppm, except for one sample); and contain several inherited zircon crystals with U-Pb isotopic ages of ~405 and 422 Ma. Thus, (i) these MS-rhyolites are probably related to hot-dry-type felsic rocks without or with poor inheritance (Miller et al., 2003); and (ii) this confirms once again that the source for MS-rhyolites could have been the Early Devonian supra-crustal (metagreywacke) material from the upper level of the Rudny-Altai basement.

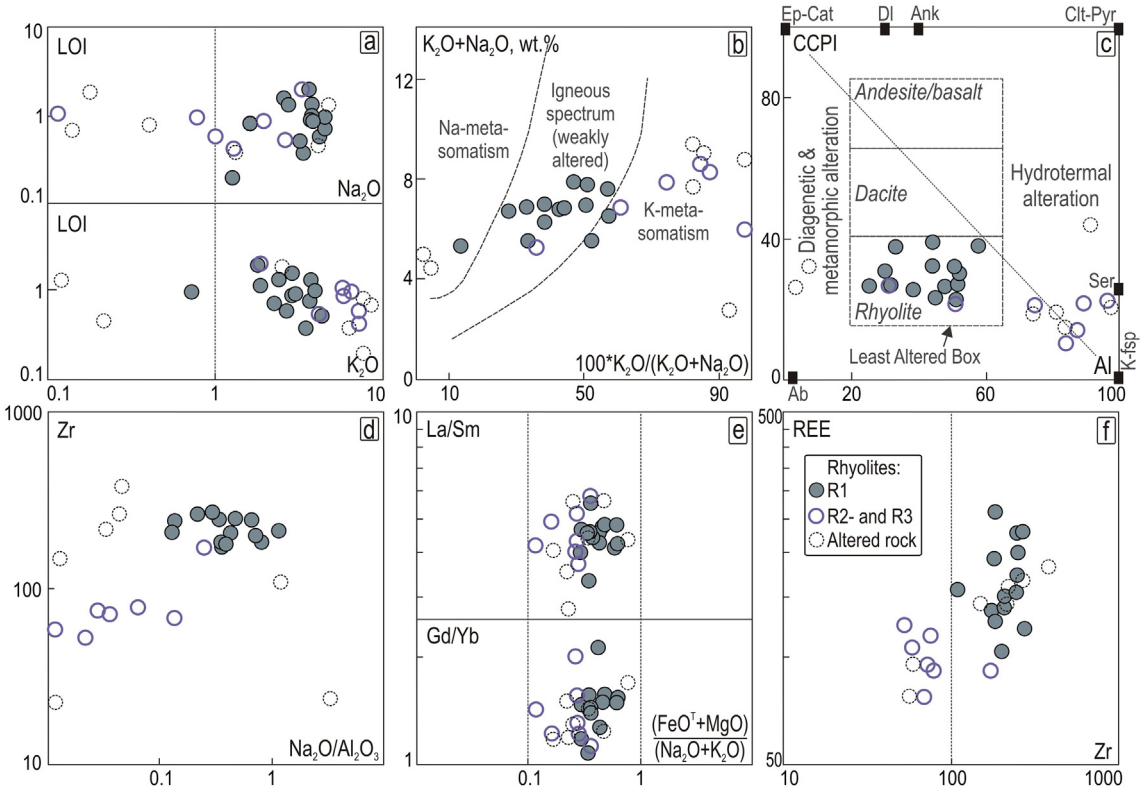

Fig. 9. Major and trace elements alteration plots for the MS-rhyolites. (a): LOI vs. Na_2O and K_2O (wt%) diagrams, indicates, that sodium alterations could be related to hydrothermal fluid, and, in contrast, potash alterations were not associated with it. (b) Igneous Spectrum diagram (Hughes, 1972), indicates, that R1-rhyolites lie inside the field weakly altered magmatic rocks; and R2- and R3-rhyolite marked inside the field K-metasomatic rocks. (c) Alteration-Box-Plot (Large et al., 2001), showing MS-rhyolites alteration trends (*CCPI* = Chlorite-Carbonate-Pyrite Index = $100 * (MgO + FeO^T)/(Mg + FeO^T + K_2O + Na_2O)$; and *Al* = Hashimoto alteration index = $100 * (K_2O + MgO)/(K_2O + MgO + Na_2O + CaO)$). The R1-rhyolites lie inside least altered box, reflecting their weakly alteration; and the R2- and R3-rhyolite lie on arrays from the least altered box toward the Ser-Kfsp side, associated with hydrothermal alteration. (d) Zr vs. Na_2O/Al_2O_3 diagram, indicating a lack of clear correlation between Zr content and sodium hydrothermal fluid for weakly altered MS-rhyolites. (e) La/Sm and Gd/Yb vs. Alteration Index diagram (Lentz, 1998), reflecting the minor modification of LREEs during chloritization (Fe + Mg) or feldspathization (Na + K) processes. (f) REEs vs. Zr (ppm) diagram indicate that REEs were relatively immobile during hydrothermal alteration, since it has the strong correlation with Zr concentrations.

6.3. Trace elements constraints

Firstly, as noted by our reviewer "There is little one can do, geochemically speaking, when dealing with weathered old volcanic rocks, except to use immobile trace elements". It has been experimentally shown (Conrad et al., 1988; Patiño Douce and Beard, 1996), that higher-silica melts can be produced by vapor-absent melting of biotite-hornblende-bearing assemblages only at low aH_2O and high temperatures (>800 °C), due to anhydrous-minerals as the dominant residual phases during melting. Alternatively, felsic orthogneisses of tonalitic to granodioritic composition, consisting of quartz-feldspathic mineralogy, as well as amphibole and biotite, and titanite, apatite, and zircon, have been recognized as one of the potential source for *A*-type granites and related volcanic rocks (e.g. Collins et al., 1982; Anderson, 1983; White and Chappell, 1983; Rutter and Wyllie, 1988; Creaser et al., 1991; Skjerlie and Johnston, 1993; Patiño Douce, 1997). In term of incompatible elements, geochemical characteristics of the MS-rhyolites ($(La/Yb)_n \sim 4$; $Zr/Y \sim 4$; $La/Sm \sim 3–5$), transitional between those of upper-crust material and mantle-derived materials (Fig. 10b–d; Sun and McDonough, 1989; Rudnick and Gao, 2003), support biotite-hornblende-bearing source. Based on Zr and Y partition coefficient between the mineral and melt ($D_{Zr}^{Amph/Melt} < 1$; $D_Y^{Amph/Melt} > 1$; e.g. Pearce and Norry, 1979; Arth, 1976), in the absence of amphibole residue, Y becomes incompatible, as is Zr, resulting in low overall Zr/Y with increasing Y. Amphibole will have the similar effect on the La/Yb ratio because LREEs are more incompatible than HREEs in this mineral; and, thus, the values of their relations should similarly approach the value close to that of the tholeiite series (Fig. 16c; Lentz, 1998). Speaking of LREEs, they have a minor dependence on fractionation of phenocryst phases such as quartz and feldspars in granite systems, but are strictly controlled by the melting of biotite ($D_{LREE}^{Bt/Melt} > 1$; $D_{La}^{Bt/Melt} \gg D_{Sm}^{Bt/Melt}$), and have a dependence on the stability of some accessory phases, such as alanite and monazite (Mahood and Hildreth, 1983). In general, the Yb vs. La/Yb diagram (Fig. 16c) indicates that partial melting of amphibole-bearing source (Beard and Lofgren, 1991) rather than hypothetical fractional differentiation of minerals in viscous high-silica magma played a dominant role in the evolution of the R1-rhyolites.

Secondary, if we consider the mineral vectors in the system of La vs. La/Yb, reflecting the relationship between geochemical indices and fractionation, the involvement of minor amounts of accessory phases in the petrogenesis of these rhyolites is also an unlikely scenario (Fig. 16d). The diagram La vs. La/Sm (Fig. 16e) shows that R1-rhyolites have a cogenetic distribution with vector reflecting the partial melting of a biotite-containing source (Koester et al., 2002). Although it is clear that the compositions of R3-rhyolites again behave in some other way. In general, we believe that some of the processes associated with high-temperature melting of metagreywacke materials or felsic meta-igneous rocks in the shallow-crustal level played a major role in the origin of MS-rhyolites.

6.4. Mechanism of the MS-rhyolite formation

Firstly, the geotectonic environments in favour of the widespread high-silica bimodal-type rhyolitic magmatism are usually associated with episodes of extensional geodynamic activity of rifted mature island arcs, rifted continental margin and marginal back-arc basin, or within-plate extensional settings, in contrast to the compositional continuum in normal subduction environments (Gribble et al., 1996; Lentz, 1998;

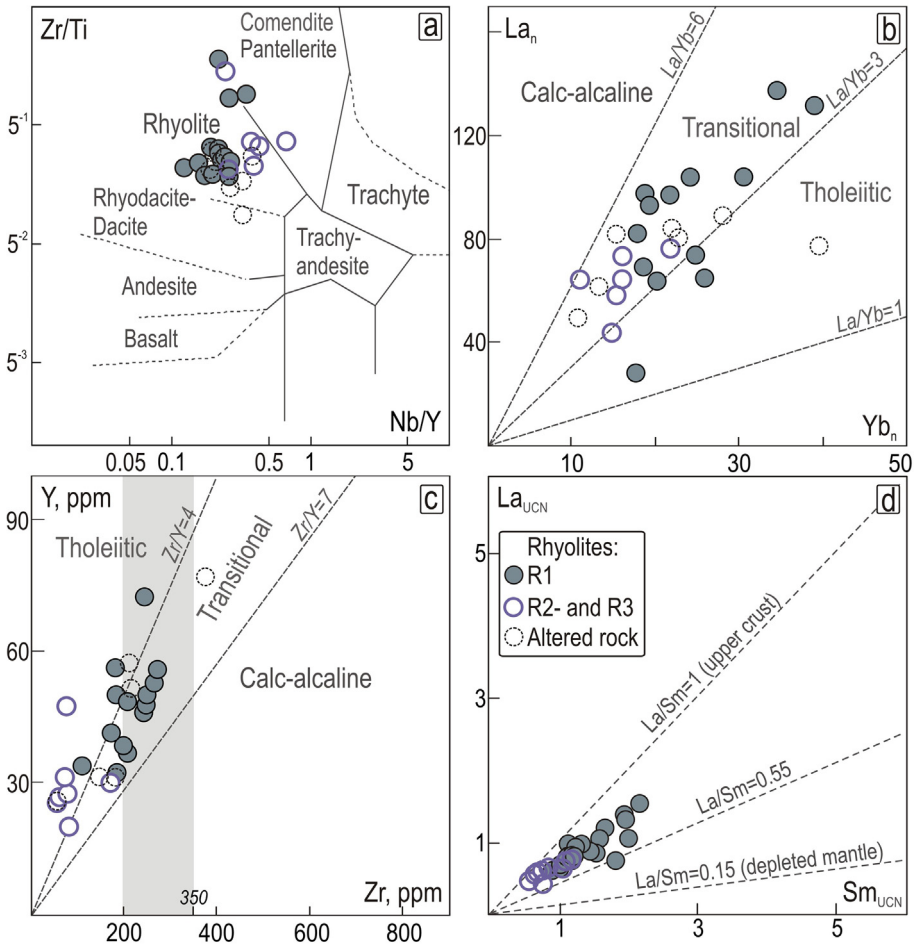

Fig. 10. Trace element classification of the MS-rhyolites. (a) Zr/TiO_2-Nb/Y (Winchester and Floyd, 1977); (b) La_n vs. Yb_n; (c) Y vs. Zr (ppm); and (d) La_{ucn} vs. Sm_{ucn} diagrams (Lentz, 1998; Piercey et al., 2008), illustrating the transitional geochemical characteristics of MS-rhyolites between mantle-derived and upper crust material. UCN = Upper crust normalized (Rudnick and Gao, 2003); values for Depleted mantle and Chondrite are from Sun and McDonough (1989).

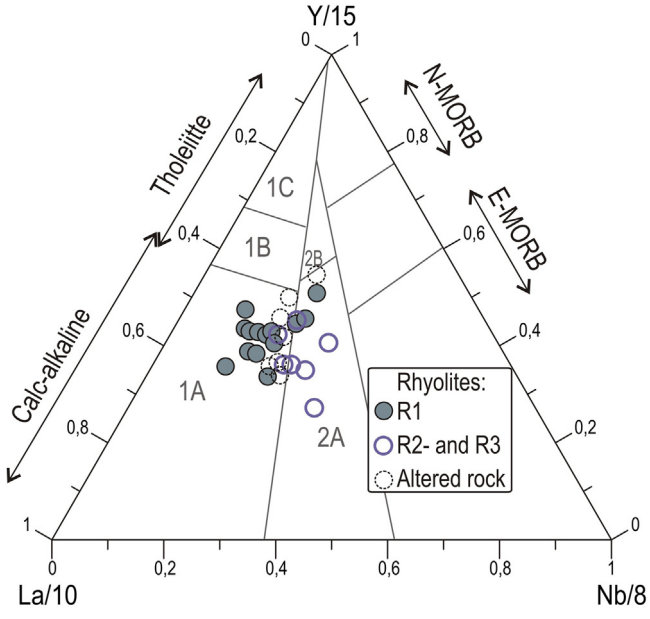

Fig. 11. Tectonic discriminant diagram La-Y-Nb (Cabanis and Lecolle, 1989), illustrating the transitional geochemical characteristics of MS-rhyolites between normal arc-related and within-plate series. 1A – calc-alcalaine series; 1B – calc-alkaline and tholeiite series; 1C – arc-related tholeiitic series; 2A – within-plate series.

Barrie and Hannington, 1999; Orozco-Esquivel et al., 2002; Bachmann and Bergantz, 2004, 2008; Piercey et al., 2006; Galley et al., 2007; Gaboury and Pearson, 2008; Tamura et al., 2009; Deering et al., 2010). A huge contribution to understanding the processes of petrogenesis and evolution of felsic magmatism was made by Bachmann and Bergantz (2008), and Deering et al. (2008, 2010). They showed that it is mainly generated by extraction of viscous melts from solid residues either in (i) long-lived crystallizing mush zones fed by mafic to intermediate magmas (dominantly down-temperature evolution with residual silicic melt), or in (ii) partial melting zones within the crust (dominantly up-temperature evolution with newly formed silicic melt). In the first case, dominated by flux melting of the supra-subduction mantle lead to generation of the cold-oxidized felsic magmas. As noted (Orozco-Esquivel et al., 2002), high-silica rhyolite or crystal-poor rhyolite is extracted by squeezing of the partly crystallized mush, percolates through pores and fractures, concentrates in small pockets and ascends to its final emplacement level using the existing plumbing system. However, in the Rudny Altai there are no low-silica granitoids, syngenetic to R1-rhyolite, which could be considered as enriched in crystals cumulated material originating from crystalline mushes (Kuibida et al., 2015). In second case, depending on the decompression melting of the mantle (higher T and/or lower fO_2/aH_2O) lead to origin of the hot-reduced felsic magmatism. Extensional regimes where major crustal fracturing may occur, controls injection and emplacement of the basic magmas into the different levels of continental crust, producing volumetric melting of the crustal material. In these conditions the high temperatures and low to moderate water contents felsic magmas are relatively fluid,

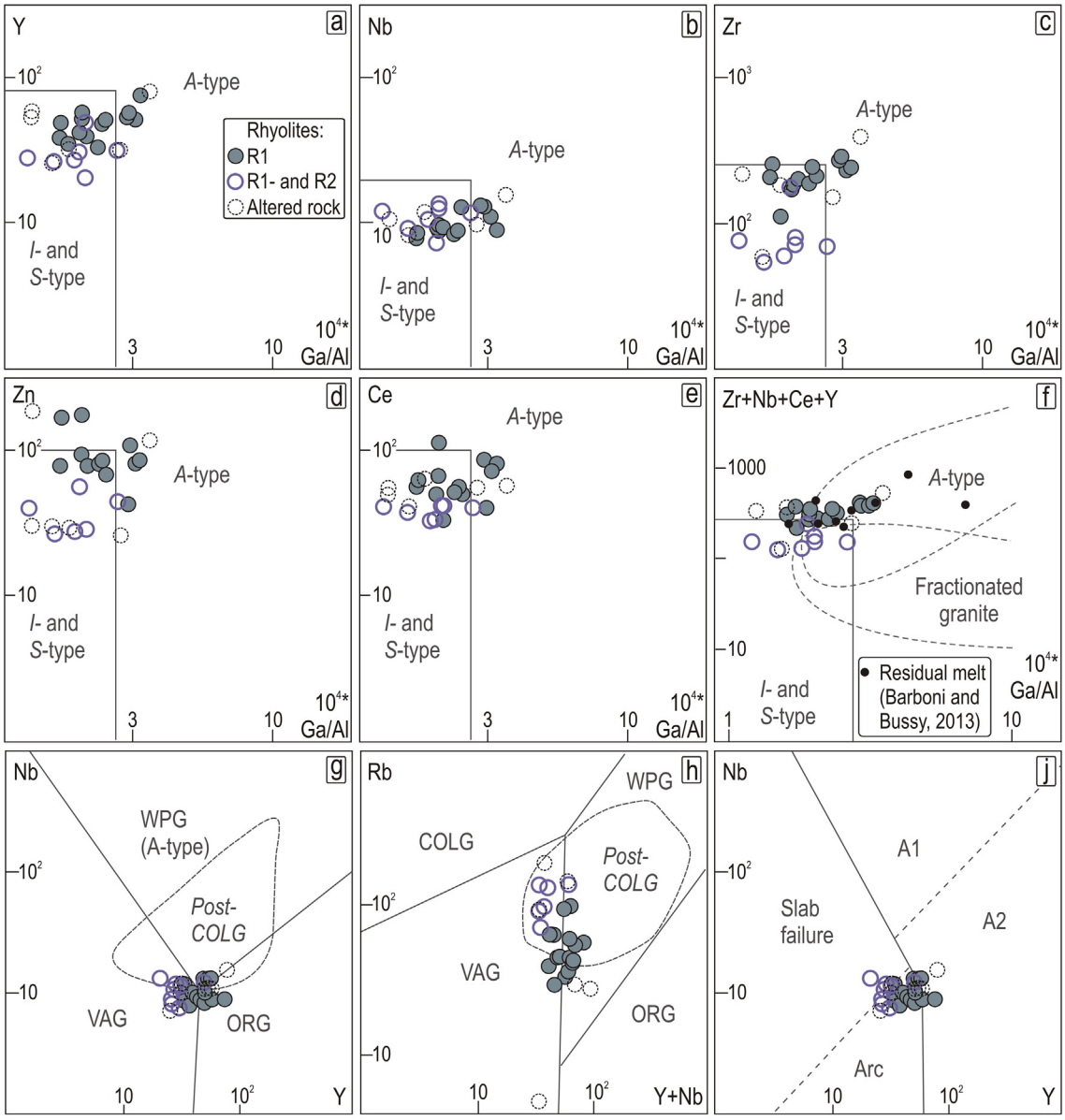

Fig. 12. Tectonic discriminant diagrams. (a–f) Y, Nb, Zr, Zn, Ce and Zr + Nb + Ce + Y vs. $10^4 * Ga/Al$ diagrams (Whalen et al., 1987; Sylvester, 1989; Wu et al., 2017), showing *A*-type evolutionary trend of the MS-rhyolites. (g–j) Nb vs. Y and Rb vs. Y + Nb diagrams (Pearce et al., 1984; Whalen and Hildebrand, 2019), illustrating the transitional geochemical characteristics of MS-rhyolites between normal arc-related and within-plate series, and the fact that they do not belong to compositional field of the slab-failure-related series. SYNCOLG = syn-collisional granites, WPG = within-plate granites, ORG = ocean ridge granites, VAG = volcanic arc granites.

highly mobile melts, able to reach very shallow depths in the crust (Clemens et al., 1986). Accordingly, the rapid extraction of magma from its source and ascent to the surface and probably inhibited its stagnation in magma chambers, contributes to (i) non-equilibrium melt generation conditions; and (ii) limited degree of assimilation and fractional crystallization, which are important factors affecting the compositional evolution of magma. Although there may be transitional varieties between those generated by mantle upwelling and those formed in arc-related environments (Bachmann and Bergantz, 2008; Deering et al., 2008).

Secondary, the trace-element concentrations and their elemental ratios are a reflection of melting reactions, related to intensive parameters (P, T, fO_2, aH_2O) and controlled by the equilibrium between melt and residual assemblage in different source region and geotectonic environments. The distinctly different compositions (REEs, HFSEs) between the two geochemical types of the MS-rhyolites may reflect the difference in their petrogenetic histories. At first sight, the REE-patterns of the R1-rhyolites has some similarities to those of wet-cold-oxidized felsic magmas (Fig. 15c), suggesting that the melting of the source region occurred under conditions resemble to those of the subduction volatile-rich system (Bachmann and Bergantz, 2008; Deering et al., 2010). However, R1-rhyolites were produced under relatively more reducing conditions, resulting in: (i) an increase in MREEs and Y, Zr, and Zr/Y ratios; and (ii) low crystallinity and dominance of anhydrous phases. For example, Deering et al. (2008) showed distinctive geochemical features between normal arc-related wet-cold-oxidized felsic magmas and reduced arc-related extensional felsic magmas, by the example of Taupo Volcanic Zone, New Zealand rhyolites (Fig. 15c). The seagull-like REE-patterns of the R2- and R3-rhyolites resemble those of rhyolites formed in dry reduced crustal conditions associated with increase in temperature induced by thermal input from the underlying hot mantle (Wilson et al., 2005); Fig. 15d. Felsic magmas with such geochemical characteristics are commonly attributed to rift-related areas of mantle upwelling, such as hotspots, continental rifts, and mid-ocean ridges (Bachmann and Bergantz, 2008; Deering et al., 2010), although noted also for the back-arc basin, as summarized in (Barboni and

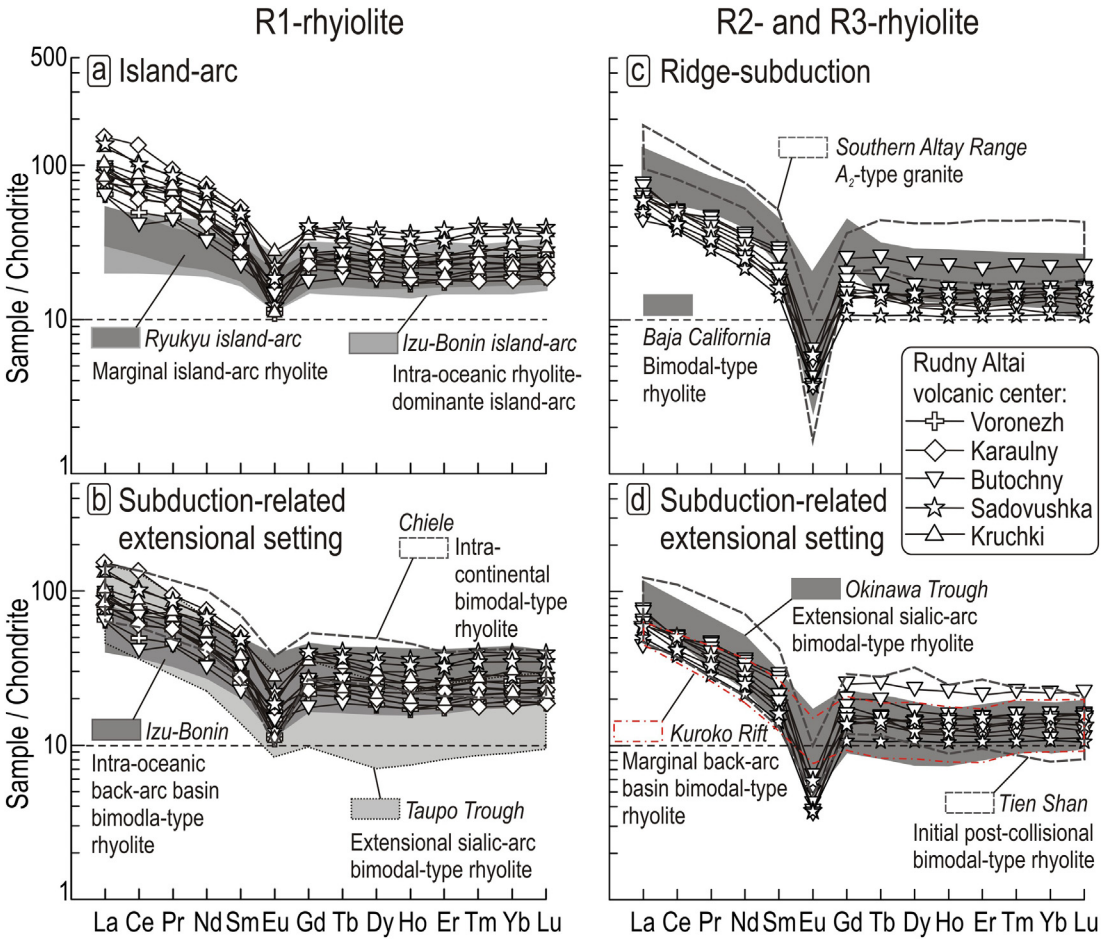

Fig. 13. Chondrite-normalized REEs diagrams (Sun and McDonough, 1989) for the MS-rhyolites, in comparison with rhyolites from (a) rhyolite-dominate intra-oceanic arc (Tamura et al., 2009), and marginal island-arc (Shinjo and Kato, 2000); (b) intra-oceanic back-arc basin (Tamura et al., 2009); rifted mature island-arc (Deering et al., 2011), and continental-margin extensional setting (Morata et al., 2000); (c) initial ridge-subduction setting (Johnson and O'Neil, 1984; Cole and Basu, 1992; Shen et al., 2011); (d) initial post-collisional setting (Chen et al., 2011), and marginal back-arc basin (Shinjo and Kato, 2000; Yamada et al., 2012). These diagrams illustrate that the REE-patterns of the MS-rhyolites are most related to those of the bimodal associations of the continental-margin extensional setting, rifted mature island-arc and marginal back-arc basin settings; and from some post-collision settings.

Bussy, 2013). Interestingly, although R2- and R3-rhyolites have contrast specificity of alkalis, but they have close similarity of REE-patterns, common low La/Sm ratios and Zr concentrations, which suggests their genetic relationship with each other. In the simplifying assumptions, the following two-stage petrological model is proposed: initial non-equilibrium melting at deeper hot levels, and subsequent melt segregation and degassing at subsurface levels. Previous studies indicate that Zr- and LREEs-undersaturated dry crustal high-K rhyolites have similar REE-patterns, and can be produced as a result of high temperature water-undersaturated disequilibrium melting, in case of melt extraction from its residuum occurred faster than extensive dissolution of accessory phases (Fig. 15d; Watt and Harley, 1993; Orozco-Esquivel et al., 2002). In the shallow-crustal levels, further segregation of parent magma into two contrasting potash-rich and sodium-rich types magmas could occur, as a result of the abrupt "dehumidification" of volatiles-rich magmatic chamber during its decompression and degassing (Abramov, 2004; Samuel et al., 2007). It is suggested that the active unloading of the magmatic system in many cases leads to the loss of volatile components even before the final crystallization of magma, and results in its segregation into two melts, the first of which, more potassium, accumulates in the lower part of the magmatic chamber, and the second, more sodium, saturated with volatile components and mobile, is injected into the host rocks (Inshin, 1972; Avdonin, 1975; Samuel et al., 2007). For example, some extreme high-Na rhyolites were interpreted as residual melt extracted from partially crystallized granite-like mush (ca. 50% of K-feldspar and quartz, and minor biotite), at a late stage of crystallization (Fig. 15d; Barboni and Bussy, 2013). This scenario is supported by the aplitic petrographic texture of the Na-rich R2-rhyolites, which could represent a melt removed from the magmatic chamber during its depressurization; and, in contrast, the porphyritic type potash-rich R3-rhyolite are in association with magmatic breccia that could represent early magmatic accumulation.

Thirdly, we believe that in the course of the long evolution of the volcanic system felsic magmas with island-arc-like geochemical features may change to rift-like one in response to the changes in the crustal architecture and magnitude of extension in the lithosphere (e.g. Gribble et al., 1996; Deering et al., 2010). In other words, we believe that arc-like extensional R1-rhyolite formed immediately after the beginning of rifting, and widespread upper crustal melting occurred under relatively more reduced conditions than the formation of wet-cold-oxidized magma in normal volatile-rich supra-subduction systems (Fig. 17a). The generation of rift-like R2- and R3-rhyolites occurred under dry and/or non-equilibrium conditions, synchronously with the rise in the upper crust of the Givetian-Fransian basic magmas, as a result of the prolonged strike-slip deformation, the Alei pull-apart basin opening, active lithospheric extension and high thermal input from the underlying hot mantle (Fig. 17b). We can draw an important preliminary conclusion that the initial rifting in the Rudny Altai could have started in the Late Emsian – Early Eifelian, since R1-rhyolites bear some arc-like geochemical signatures, but formed under more reduced conditions. In addition, although in the evolution of the entire volcanic system there have been changes in the mechanisms of magma generation, it has

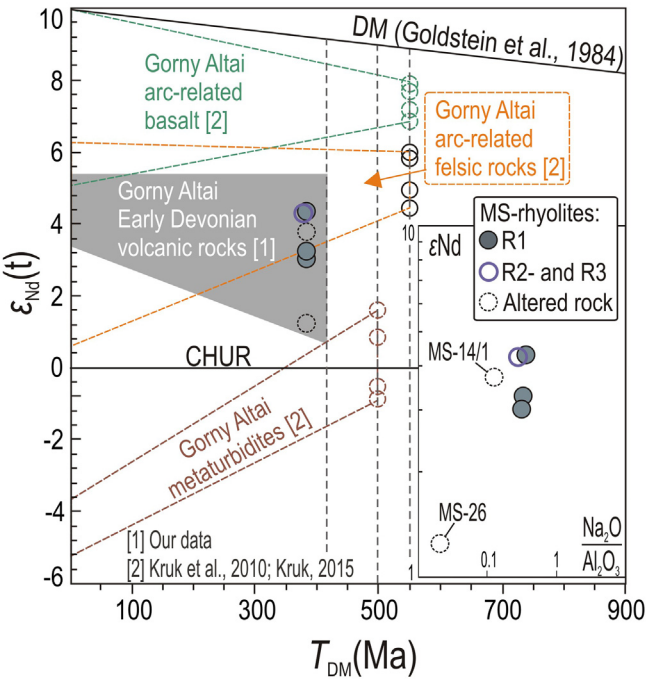

Fig. 14. εNd(t) vs. T_{DM} (Ma) age plot for the MS-rhyolites. Data for the Gorny Altai arc-related Cambrian volcanic rocks and Ordovician metaturbidites are according to (Kruk et al., 2010; Kruk, 2015); those for the Early Devonian volcanic rocks from the Altai-Mongolian block (from basalt to rhyolite) are ours. For details of data selection see Table 3. Inset with the diagram εNd(t) vs. Na_2O_3/Al_2O_3 illustrates the composition of rocks altered and unaltered by potassium metasomatism.

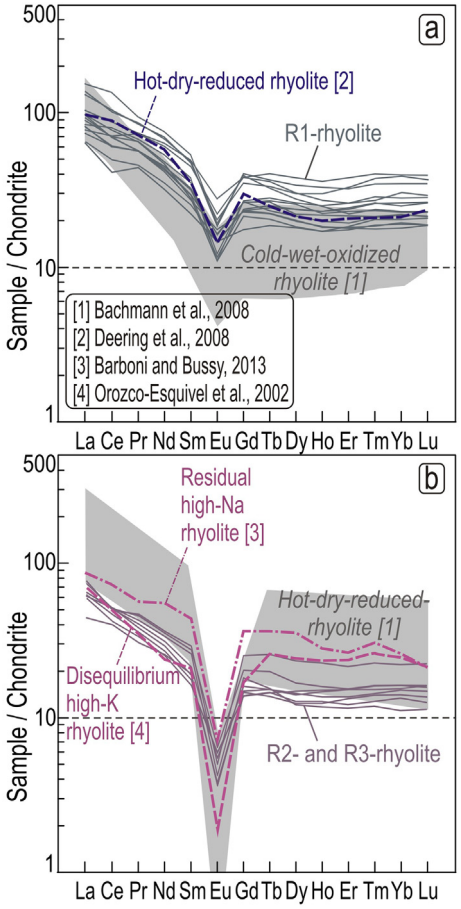

Fig. 15. (a, b) Chondrite-normalized REEs diagrams (Sun and McDonough, 1989), for the MS-rhyolites, in relative to cold-wet-oxidized and hot-dry-reduced rhyolites. These diagrams show that the REE-patterns of the R1-rhyolites have affinity with some of the transitional hot-dry-reduced rhyolites of subduction-related extensional settings. The REE-patterns of the R2- and R3-rhyolites resemble those of some Na-rich residual rhyolites and K-rich disequilibrium rhyolites, also marked for subduction-related extensional settings. References to data sources are shown in the figure.

not affected the spatial distribution of the emplaced magmas, which indicates the long-living nature of the permeable tectonic zones of the Alei pull-apart structure and emphasizes its rift-setting.

6.5. Tectonic implication

Firstly, the Altai orogen was under a convergent environment in the Devonian, but debate exists on whether it was an active continental margin of Andean-type, that evolved in the sialic island arc of Japan-type (Rotarash et al., 1982; Shokalsky et al., 2000; Glorie et al., 2011; Chen et al., 2019), or a continental margin rift setting (Kozlov, 1995; Bespaev et al., 1997; Promyslova, 2004). Some geologists consider that the frontal part of the Altai continental margin resembles Okinawa Through behind the Ryukyu SW of Japan island arc or Taupo Rift of the North Island of New Zealand in Tonga-Kermadek arc system (Karaulov et al., 1992). A ridge subduction was proposed for the continuation of the Rudny-Altai volcanic belt in the SE (Ashele basin, Xinjiang, China; e.g. Wan et al., 2010; Wu et al., 2015; Yang et al., 2018), in such as scenario hot oceanic plate was subducted and subsequent slab window was formed (e.g. Ma et al., 2018; and reference above). It should be noted that the question of the collapse of the overthickened orogen was never considered in any of the geodynamic models, which would inevitably have to happen if the Andean-type subduction orogen evolved. In the light of the newest world geodynamic models, it is widely known that the collapse of the Andean orogens on both sides of the Pacific was accompanied by lithospheric delamination and asthenospheric upwelling (e.g. Wang et al., 2007; Xu et al., 2006; Zhu et al., 2010), and generation of adakite-like magmas as a result of partial melting of overthickened continental crust (Foster et al., 2001; Kapp et al., 2002; DeCelles, 2004). However, Devonian adakites (Scherba et al., 1998; Murzin et al., 2001), have not yet been found in either the Russian or the Kazakhstan parts of the Altai orogen, as the evidence of the its collapse; or subduction spreading zone and slab melting in subduction windows (e.g. Defant and Drummond, 1993; Drummond et al., 1996; Sajona et al., 2000). It is possible that they do exist, but have not yet been discovered due to the lack of a detailed regional analytical database for these territories. It is also possible that at the post-subduction stage the frontal part of Rudny Altai was fragmented and moved by large-amplitude sinistral deformation (Buslov, 2011), as evidenced, for example, by an anomalously distance of ~20 km between the Rudny Altai volcanic belt and Irtysh Shear Zone.

Secondary, the formation of the volcanic belt of the NW Rudny Altai could be related to a continental-margin region extension, induced by a distant spreading of oceanic ridge, consistent with its sub-parallel orientation to the continental margin (e.g. Ma et al., 2018). For example, Tertiary rift-like felsic magmatism in the Mesa Central, Mexico, occurred in the rear part of Baja California (Orozco-Esquivel et al., 2002). On the other hand, the ridge-subduction-related processes should have occurred later than the formation of a normal supra-subduction volcanic belt; otherwise it is difficult to imagine the subduction of the spreading zone without subduction the oceanic plate. However, in the Rudny Altai there is no normal arc-related volcanism occurred before the formation of the bimodal-type MS-rhyolites (~390–380 Ma), and there is a genetic link of volcanism and volcanogenic massive sulphide deposits with rifting. Thus, these do not contribute a geodynamic setting of normal island arc.

Thirdly, it could be a reflection of an oblique subduction and slab roll-back processes of "extension accretionary orogen" (Collins, 2002), that induced regional extension of the continental margin. For example, the Early Devonian initialization of the Altai active margin occurred

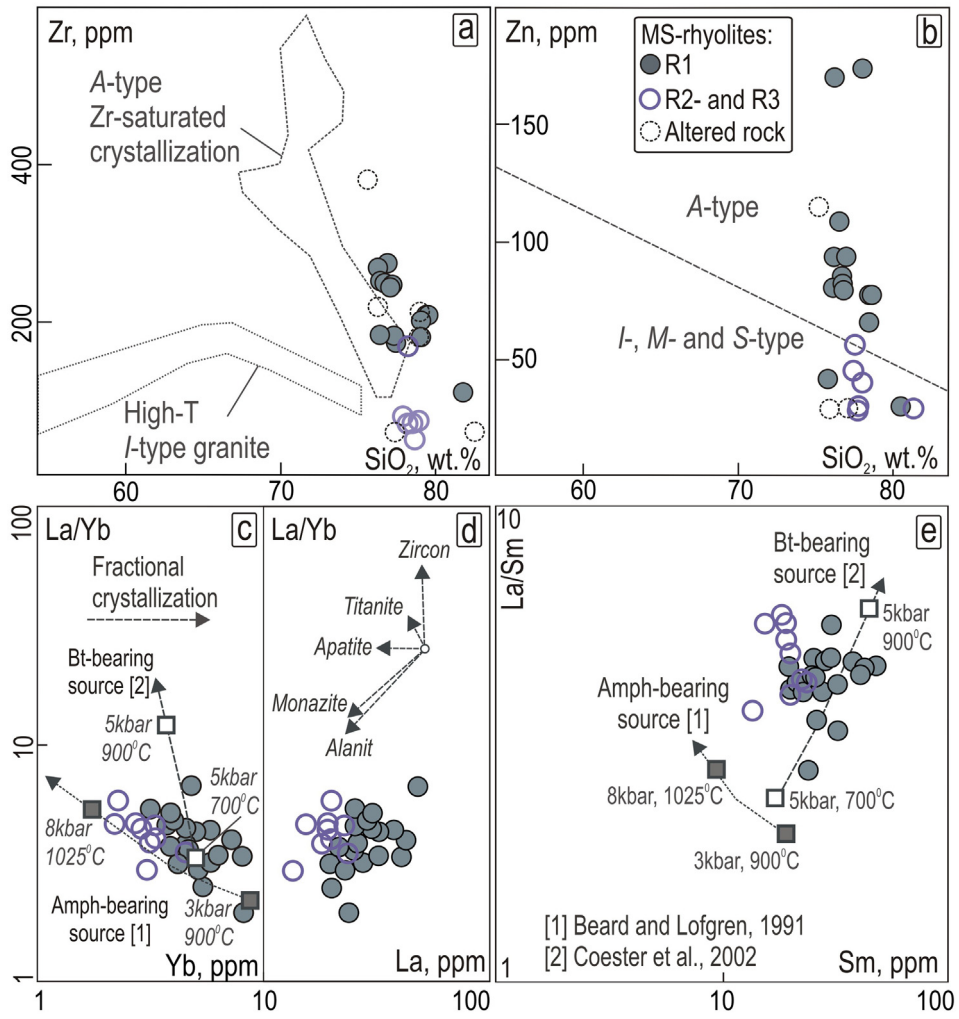

Fig. 16. (a) Zr (ppm) vs. SiO_2 (wt%) content for *A*- and *I*-type granites at Zr-saturated crystallization (King et al., 1997). The chemical trends show continuously decreasing Zr with increasing SiO_2 and indicating derivation from a quartz-feldspathic source and primary zircon saturation. (b) Zn vs. SiO_2 diagram for *A*- and *M*-, *I*- and *S*-type granites, illustrating the relationship between high Zn contents and high-*T A*-type felsic magmas (Lentz, 1998). (c) La/Yb vs. Yb plot showing relationship between the change of REEs of MS-rhyolites and dehydration melting amphibole-bearing source, with a non-garnet residual phase (Beard and Lofgren, 1991). (c) La/Yb vs. La plot showing, that variations of these elements are not controlled by fractionation of accessory phases (Li et al., 2013); (d) La/Sm vs. Sm plot showing the relationship between the change of REEs of MS-rhyolites and the dehydration melting of a biotite-bearing source, with a non-garnet residual phase (Koester et al., 2002).

within the terrain-orogenic belt (Gorny Altai) of the Siberian continent, ~20 Ma before the formation of the volcanic belt on the front of the active margin (Rudny Altai), as it follows from numerous geochronological data (Shokalsky et al., 2000; Babin et al., 2004; Glorie et al., 2011; Cai et al., 2014; Krupchatnikov et al., 2018; Chen et al., 2019); Fig. 1. This geological record resembles the Japan magmatic arc formed at a terrestrial continental margin via a stage of spreading in a back-arc basin followed by multiple stages of submarine rifting (e.g. Yamada et al., 2012). It is assumed the Rudny-Altai block is a back-arc basin fragment formed after the destruction of the Siberian passive margin in the Early Devonian. Based on all the lines of evidence presented in this study, we propose extension regime in the transition area between the island-arc and back-arc basin for the origin of the NW Rudny Altai volcanic belt. The retreat and change in the angle of the subducting plate (from flat to steep) may be one of the causes for the migration of volcanism from the continent to the ocean at the Altai convergent margin.

7. Conclusion

Our new field and geochemical data for the Devonian magmatism in the NW Rudny Altai volcanic belt (Russia) suggest:

(1) Two different geochemical types of subvolcanic silica-rich intrusions (MS-rhyolites) were emplaced at ~390 and 380 Ma, respectively. They were triggered by intensive melting of the upper crust materials beneath the Rudny Altai. The consistent formation of the arc-like rhyolites (R1) and then rift-like rhyolites (R2 and R3) suggests progressive rifting.

(2) The island-arc-like R1-rhyolite formed immediately after the beginning of rifting due to widespread crustal melting under reduced conditions. The rift-like R2- and R3-rhyolites were generated under non-equilibrium conditions, synchronously with the ascent of basaltic melts to the upper crust as a result of lithospheric extension and high thermal input from the underlying hot mantle.

(3) The RA-rhyolites formation was related to rifting in the transition area between the island-arc and back-arc basin, ~20 Ma after the initial continental-margin region extension.

Declaration of competing interest

The authors declare that they have no known competing financial interests or personal relationships that could have appeared to influence the work reported in this paper.

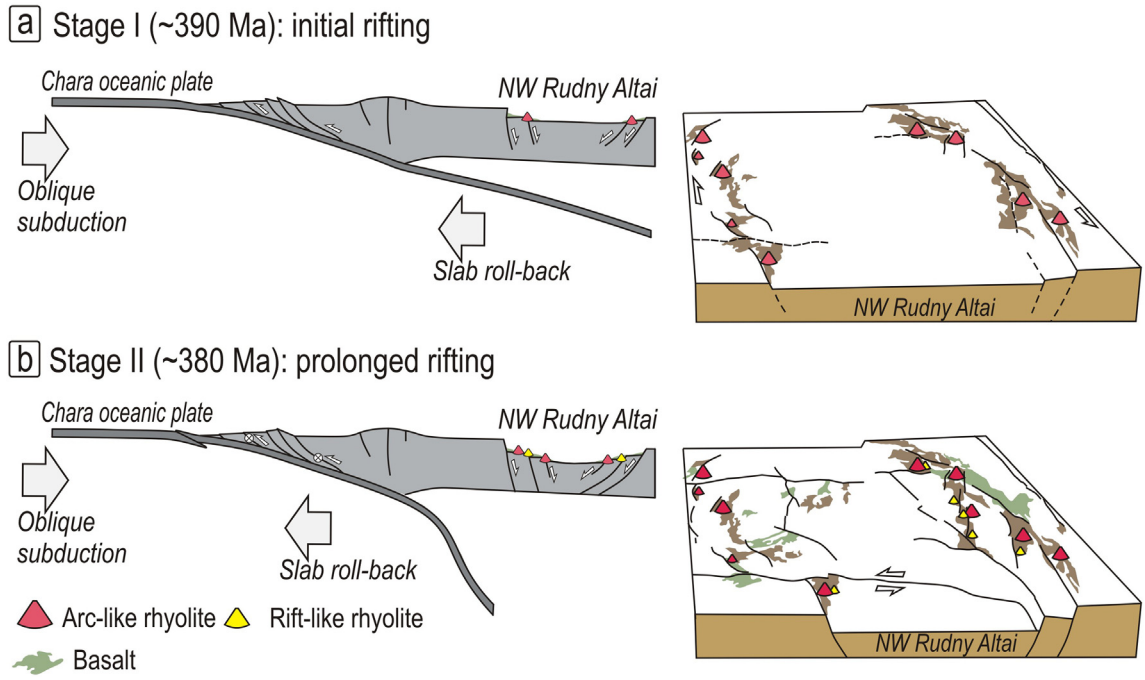

Fig. 17. Schematic cartoon illustrating conceptual authors scenario at Early – Middle Devonian evolution of the NW Rudny Altai. It is suggested that retreat of the subducting plate may cause intensive extension of the continental margin, and large-scale crustal anatexis resulting in the formation of a large volume of rhyolites. The first stage (a) reflects the formation of arc-like extensional R1-rhyolite formed immediately after the beginning of rifting. The second stage (b) reflects the generation of rift-like R2- and R3-rhyolites occurred under more dry and/or non-equilibrium conditions, synchronously with the ascent in the upper crust of the Givetian–Fransian basic magmas, as a result of the active lithospheric extension and high thermal input from the mantle.

Acknowledgments

Writing this paper would be impossible without years of the hard field and laboratory work of skillful geologists from Russia, China and Kazakhstan. We are sincerely grateful to the reviewers who have enabled us to make this paper better. The study was carried out as part of a basic research program at the Ministry of Science and Education of the Russian Federation (Projects Nos. 14.Y26.31.0018), the Russian Foundation for Basic Research (project no. 16-05-01021), Hong Kong RGC grants 17302317 and 17303415; and according to the plan of the State Assignment of the Institute of Geology and Mineralogy, Siberian Branch, Russian Academy of Sciences.

References

Abramov, S.S., 2004. Formation of fluorine-rich magmas by fluid filtration through silicic magmas: Petrological and geochemical evidence of metamagmatism. Russian Petrology 12 (1), 17–36.
Alt, J.C., Teagle, D.A., 2003. Hydrothermal alteration of upper oceanic crust formed at a fast-spreading ridge: mineral, chemical, and isotopic evidence from ODP Site 801. Chem. Geol. 201 (3–4), 191–211.
Anderson, J.L., 1983. Proterozoic anorogenic plutonism of North America. In: Medaris, L.G., Byers, C.W., Nickelson, D.M., Shanks, W.C. (Eds.), Precambrian Geology: Selected Papers From an International Symposium: Geological Society of America Memoir. 161, pp. 133–154.
Arth, J.G., 1976. Behavior of trace elements during magmatic processes – a summary of theoretical models and their applications. United States Geological Survey 4 (1), 41–47.
Avdonin, V.V., 1975. Feature of Segregation in the Middle Devonian Volcanic Rocks of Acid Composition of Leninogorsk District, Rudny Altai. (Reports of). Moscow University, p. 6.
Ayers, J.C., Zhang, L., Luo, Y., Peters, T.J., 2012. Zircon solubility in alkaline aqueous fluids at upper crustal conditions. Geochim. Cosmochim. Acta 96, 18–28.
Babin, G.A., Vladimirov, A.G., Kruk, N.N., Sergeev, S.A., Sennikov, N.V., Gibsher, A.S., Sovetov, K., 2004. Age of the initiation of Minusa Basins, Southern Siberia. Dokl. Earth Sci. 395 (3), 307–310.
Bachmann, O., Bergantz, G.W., 2004. On the origin of crystal-poor rhyolites: extracted from batholithic crystal mushes. J. Petrol. 45 (8), 1565–1582.
Bachmann, O., Bergantz, G.W., 2008. Rhyolites and their source mushes across tectonic settings. J. Petrol. 49 (12), 2277–2285.
Barboni, M., Bussy, F., 2013. Petrogenesis of mag matic albite granites associated to cogenetic A-type granites: Na-rich residual melt extraction from a partially crystallized A-type granite mush. Lithos 177, 328–351.
Barrett, T.J., MacLean, W.H., 1999. Volcanic sequences, lithogeochemistry, and hydrothermal alteration in some bimodal volcanic-associated massive sulfide systems. Rev. Econ. Geol. 8, 101–131.
Barrie, C.T., Hannington, M.D., 1999. Classification of volcanic-associated massive sulfide deposits based on host-rock composition. Rev. Econ. Geol. 8, 1–11.
Battey, M.H., 1955. Alkali metasomatism and the petrology of some keratophyres. Geol. Mag. 92 (2), 104–126.
Beard, J.S., Lofgren, G.E., 1991. Dehydration melting and water-saturated melting of basaltic and andesitic greenstones and amphibolites at 1, 3, and 6. 9 kb. J. Petrol. 32 (2), 365–401.
Bespaev, H.A., Polyansky, N.V., Ganzhenko, G.D., 1997. Geology and Metallogeny of the Southwestern Altai (Territory of Kazakhstan and China). Gylym, Almaty.
Black, L.P., Kamo, S.L., Allen, C.M., Davis, D.W., Aleinikoff, J.N., Valley, J.W., Mundil, R., Campbell, I.H., Korsch, R.J., Williams, I.S., Foudoulis, C., 2004. Improved Pb-206/U-218 microprobe geochronology by the monitoring of a trace-element-related matrix effect; SHRIMP, ID-TIMS, ELA-ICP-MS and oxygen isotope documentation for a series of zircon standards. Chem. Geol. 205, 115–140.
Boehnke, P., Watson, E.B., Trail, D., Harrison, T.M., Schmitt, A.K., 2013. Zircon saturation revisited. Chem. Geol. 351, 324–334.
Buslov, M.M., 2011. Tectonics and geodynamics of the Central Asian Fold belt: the role of Late Paleozoic large-amplitude strike-slip faults. Russ. Geol. Geophys. 52 (1), 52–71.
Buslov, M.M., Saphonova, I.Y., Watanabe, T., Obut, O.T., Fujiwara, Y., Iwata, K., Semakov, N.N., Sugai, Y., Smirnova, L.V., Kazansky, A.Y., Itaya, T., 2001. Evolution of the Paleo-Asian Ocean (Altai-Sayan, Central Asia) and collision of possible Gondwana-derived terranes with the southern marginal part of the Siberian continent. J. Geosci. 5, 203–224.
Buslov, M.M., Watanabe, T., Fujiwara, Y., Iwata, K., Smirnova, L.V., Safonova, I.Y., Semakov, N.N., Kiryanova, A.P., 2004. Late Paleozoic faults of the Altai region, Central Asia: tectonic pattern and model of formation. J. Asian Earth Sci. 23, 655–671.
Cabanis, B., Lecolle, M., 1989. The La/10-Y/15-Nb/8 diagram: a tool for distinguishing volcanic series and discovering crustal mixing and/or contamination. Comptes Rendus de l'Academie des Sciences. Serie 2. Science de la Terre 309, 20.
Cai, K., Sun, M., Yuan, C., Long, X., Xiao, W., 2011. Geological framework and Paleozoic tectonic history of the Chinese Altai, NW China: a review. Russ. Geol. Geophys. 52 (12), 1619–1633.
Cai, K., Sun, M., Xiao, W., Buslov, M.M., Yuan, C., Zhao, G., Long, X., 2014. Zircon U-Pb geochronology and Hf isotopic composition of granitiods in Russian Altai Mountain, central Asian orogenic belt. Am. J. Sci. 314 (2), 580–612.
Castro, A., Corretgé, G.L., El-Biad, M., El-Hmidi, H., Fernandez, C., Patino-Douce, A.E., 2000. Experimental constraints on Hercynian anatexis in the Iberian Massif, Spain. J. Petrol. 41 (10), 1471–1488.
Chappell, B.W., 1999. Aluminium saturation in I-and S-type granites and the characterization of fractionated haplogranites. Lithos 46 (3), 535–551.
Chappell, B.W., White, A.J.R., 1992. I-and S-type granites in the Lachlan Fold Belt. Geol. Soc. Am. Spec. Pap. 272, 1–26.

Chen, X., Shu, L., Santosh, M., 2011. Late Paleozoic post-collisional magmatism in the Eastern Tianshan Belt, Northwest China: new insights from geochemistry, geochronology and petrology of bimodal volcanic rocks. Lithos 127 (3–4), 581–598.
Chen, Y., Xiao, X., Windley, B.F., Zhang, J., Zhou, K., 2017. Late Devonian-early Permian subduction-accretion of the Zharma-Saur oceanic arc, West Junggar (NW China): Insights from field geology, geochemistry and geochronology. J. Asian Earth Sci. 145, 424–445.
Chen, M., Sun, M., Buslov, M.M., Zheng, J., Zhao, J., Cai, K., Kulikova, A.V., 2019. Devonian continental arc intermediate-felsic magmatism in the Gorny Altai terrane, northwestern Central Asian Orogenic Belt: heterogenous crustal melting and input of mantle melts. Lithos 332, 175–191.
Chernov, V.I., 1974. Volcanogenic Formations and porphyry intrusions in Rudny Altai (in Russian). Nauka, Moscow 264.
Clemens, J.D., Holloway, J.R., White, A.J.R., 1986. Origin of an A-type granite; experimental constraints. Am. Mineral. 71 (3–4), 317–324.
Cole, R.B., Basu, A.R., 1992. Middle Tertiary volcanism during ridge-trench interactions in western California. Science. 258 (5083), 793–796.
Collins, W.J., 2002. Nature of extensional accretionary orogens. Tectonics 21 (4) 6-1.
Collins, W.J., Beams, S.D., White, A.J.R., Chappell, B.W., 1982. Nature and origin of A type granites with particular reference to southeastern Australia. Contrib. Mineral. Petrol. 80, 189–200.
Conrad, W.K., Nicholls, I.A., Wall, V.J., 1988. Water-saturated and-undersaturated melting of metaluminous and peraluminous crustal compositions at 10 kb: evidence for the origin of silicic magmas in the Taupo Volcanic Zone, New Zealand, and other occurrences. J. Petrol. 29 (4), 765–803.
Creaser, R.A., Price, R.C., Wormald, R.J., 1991. A-type granites revisited: assessment of a residual-source model. Geology 19 (2), 163–166.
Daly, R.A., 1914. Igneous Rocks and Their Origin. McGraw-Hill Book Company, Inc.
DeCelles, P.G., 2004. Late Jurassic to Eocene evolution of the Cordilleran thrust belt and foreland basin system, western USA. Am. J. Sci. 304 (2), 105–168.
Deering, C.D., Cole, J.W., Vogel, T.A., 2008. A rhyolite compositional continuum governed by lower crustal source conditions in the Taupo Volcanic Zone, New Zealand. J. Petrol. 49 (12), 2245–2276.
Deering, C.D., Gravley, D.M., Vogel, T.A., Cole, J.W., Leonard, G.S., 2010. Origins of cold-wet-oxidizing to hot-dry-reducing rhyolite magma cycles and distribution in the Taupo Volcanic Zone, New Zealand. Contrib. Mineral. Petrol. 160 (4), 609–629.
Deering, C.D., Cole, J.W., Vogel, T.A., 2011. Extraction of crystal-poor rhyolite from a hornblende-bearing intermediate mush: a case study of the caldera-forming Matahina eruption, Okataina volcanic complex. Contrib. Mineral. Petrol. 161 (1), 129–151.
Defant, M.J., Drummond, M.S., 1993. Mount St. Helens: potential example of the partial melting of the subducted lithosphere in a volcanic arc. Geology 21 (6), 547–550.
Dobretsov, N.L., Berzin, N.A., Buslov, M.M., 1995. Opening and tectonic evolution of the Paleo-Asian Ocean. Int. Geol. Rev. 37, 335–360.
Drummond, M.S., Defant, M.J., Kepezhinskas, P.K., 1996. Petrogenesis of slab-derived trondhjemite–tonalite–dacite/adakite magmas. Earth and Environmental Science Transactions of the Royal Society of Edinburgh. 87 (1–2), 205–215.
Eby, G.N., 1990. The A-type granitoids: a review of their occurrence and chemical characteristics and speculations on their petrogenesis. Lithos 26, 115–134.
Foster, D.A., Schafer, C., Fanning, C.M., Hyndman, D.W., 2001. Relationships between crustal partial melting, plutonism, orogeny, and exhumation: Idaho–Bitterroot batholith. Tectonophysics 342 (3–4), 313–350.
Frost, B.R., Barnes, C.G., Collins, W.J., Arculus, R.J., Ellis, D.J., Frost, C.D., 2001. A geochemical classification for granitic rocks. J. Petrol. 42, 2033–2048.
Gaboury, D., Pearson, V., 2008. Rhyolite geochemical signatures and association with volcanogenic massive sulfide deposits: examples from the Abitibi Belt, Canada. Econ. Geol. 103 (7), 1531–1562.
Galley, A.G., Hannington, M.D., Jonasson, I.R., 2007. Volcanogenic massive sulphide deposits. Mineral deposits of Canada: a synthesis of major deposit-types, district metallogeny, the evolution of geological provinces, and exploration methods. Geological Association of Canada, Mineral Deposits Division, Special Publication. 5, 141–161.
Gaskov, I.V., 2015. Specific features of pyrite ore-magmatic systems development in the island arc environments of Rudny Altai and Southern Urals. Russ. Lithosphere 2, 17–39.
Glorie, S., De Grave, J., Buslov, M.M., Zhimulev, F.I., Izmer, A., Vandoorne, W., Elburg, M.A., 2011. Formation and Palaeozoic evolution of the Gorny-Altai–Altai-Mongolia suture zone (South Siberia): zircon U/Pb constraints on the igneous record. Gondwana Res. 20 (2–3), 465–484.
Goldstein, S.J., Jacobsen, S.B., 1988. Nd and Sm isotopic systematics of rivers water suspended material: implications for crustal evolution. Earth Planet. Sci. Lett. 87, 249–265.
Gribble, R.F., Stern, R.J., Bloomer, S.H., Stüben, D., O'Hearn, T., Newman, S., 1996. MORB mantle and subduction components interact to generate basalts in the southern Mariana Trough back-arc basin. Geochim. Cosmochim. Acta 60 (12), 2153–2166.
Griffin, W.L., Powell, W.J., Pearson, N.J., O'Reilly, S.Y., 2008. GLITTER: data reduction software for laser ablation ICP-MS. In: Sylvester, P. (Ed.), Laser Ablation ICP-MS in the Earth Sciences: Current Practices and Outstanding Issues: Mineralogical Association of Canada. 40, pp. 307–311 Short Course Series.
Hart, T.R., Gibson, H.L., Lesher, C.M., 2004. Trace element geochemistry and petrogenesis of felsic volcanic rocks associated with volcanogenic massive Cu-Zn-Pb sulfide deposits. Econ. Geol. 99, 1003–1013.
Hu, A., Jahn, B.M., Zhang, G., Chen, Y., Zhang, Q., 2000. Crustal evolution and Phanerozoic crustal growth in northern Xinjiang: Nd isotopic evidence. Part I. Isotopic characterization of basement rocks. Tectonophysics 328, 15–51.
Hughes, C.J., 1972. Spilites, keratophyres, and the igneous spectrum. Geol. Mag. 109 (6), 513–527.
Inshin, P.V., 1972. Mechanisms of Magma Differentiation. Nauka, Kaz. SSR Alma-Ata.
Irvine, T.N.J., Baragar, W.R.A.F., 1971. A guide to the chemical classification of the common volcanic rocks. Can. J. Earth Sci. 8, 523–548.
Jacobsen, S.B., Wasserburg, G.J., 1984. Sm-Nd isotopic evolution of chondrites and achondrites, II. Earth Planet. Sci. Lett. 67, 137–150.
Jaffey, A.H., Flynn, K.F., Glendenin, L.E., Bentleyt, W.C., Essling, A.M., 1971. Precision measurement of halflives and specific activities of 235U and 238U. Phys. Rev. 4, 1889–1906.
Jahn, B., Wu, F., Chen, B., 2000. Granitoids of the Central Asian Orogenic Belt and continental growth in the Phanerozoic. Trans. Roy. Soc. Edinburgh 91, 181–193.
Jenner, G.A., Longerich, H.P., Jackson, S.E., Fryer, B.J., 1990. ICP-MS as a powerful tool for high precision trace element analysis in earth sciences: evidence from analysis of selected U.S.G.S. reference samples. Chem. Geol. 83, 133–148.
Jochum, K.P., Nohl, U., 2008. Reference materials in geochemistry and environmental research and the GeoReM database. Chem. Geol. 253 (1–2), 50–53.
Johnson, C.M., O'neil, J.R., 1984. Triple junction magmatism: a geochemical study of Neogene volcanic rocks in western California. Earth Planet. Sci. Lett. 71 (2), 241–262.
Kapp, J.D.A., Miller, C.F., Miller, J.S., 2002. Ireteba pluton, Eldorado Mountains, Nevada: Late, deep-source, peraluminous magmatism in the Cordilleran Interior. J. Geology 110 (6), 649–669.
Karaulov, V.B., Filatova, L.K., Nikitina, M.I., 1992. Devonian geologic formations of the Zmeinogorsk ore district (Rudny Altai). Russ. Geol. Geophys. 2, 3–10.
Kasapoğlu, B., Ersoy, Y.E., Uysal, İ., Palmer, M.R., Zack, T., Koralay, E.O., Karlsson, A., 2016. The petrology of Paleogene volcanism in the Central Sakarya, Nallıhan Region: implications for the initiation and evolution of post-collisional, slab break-off-related magmatic activity. Lithos 246, 81–98.
King, P.L., White, A.J.R., Chappell, B.W., 1997. Characterization and origin of aluminous A-type granites of the Lachlan Fold Belt, southeastern Australia. J. Petrol. 36, 371–391.
Koester, E., Pawley, A.R., Fernandes, L.A.D., Porcher, C.C., Soliani, E., 2002. Experimental melting of Cordierite Gneiss and the petrogenesis of Syntranscurrent Perfluminous granites in Southern Brasil. J. Petrol. 43 (8), 1595–1616.
Kozlov, M.S., 1995. Paleotectonic and paleovolcanism of the Middle Paleozoic of the Southwestern Altai. Russ. Geol. Geophys. 36 (12), 17–34.
Kröner, A., Kovach, V., Belousova, E., Hegner, E., Armstrong, R., Dolgopolova, A., Sun, M., 2014. Reassessment of continental growth during the accretionary history of the Central Asian Orogenic Belt. Gondwana Res. 25, 103–125.
Kruk, N.N., 2015. Continental crust of Gorny Altai: stages of formation and evolution; indicative role of granitoids. Russ. Geol. Geophys. 56 (8), 1097–1113.
Kruk, N.N., Vladimirov, A.G., Babin, G.A., Shokalsky, S.P., Sennikov, N.V., Rudnev, S.N., Serov, P.A., 2010. Continental crust in Gorny Altai: nature and composition of protoliths. Russ. Geol. Geophys. 51 (5), 431–446.
Krupchatnikov, V.I., Vrublevskii, V.V., Kruk, N.N., 2018. Early Devonian volcanics of southeastern Gorny Altai: geochemistry, isotope (Sr, Nd, and O) composition, and petrogenesis (Aksai complex). Russ. Geol. Geophys. 59 (8), 905–924.
Kuibida, M.L., 2019. Basaltic volcanism of Island-Arc–Back-Arc basin system (Altai active margin). Russian Journal of Pacific Geology 13 (3), 297–309.
Kuibida, M.L., Kruk, N.N., Shokal'skii, S.P., Gusev, N., Murzin, O., 2015. Subduction plagiogranites of Rudny Altai: age and composition characteristics. Dokl. Earth Sci. 464 (1), 914–918.
Kulkov, N.P., 1980. Lower and Middle Devonian Biostratigraphy of the Rudny Altay. 425. Academy of Sciences of the USSR Siberian Branch Institute of Geology and Geophysics. Transactioris, p. 157.
Kuznetsov, Y.A., 1964. Main Types of Magmatic Formations. Nedra, Moscow. 387.
Large, R.R., Gemmell, J.B., Paulick, H., Huston, D.L., 2001. The alteration box plot: a simple approach to understanding the relationship between alteration mineralogy and lithogeochemistry associated with volcanic-hosted massive sulfide deposits. Econ. Geol. 96 (5), 957–971.
Le Maitre, R.W.B., Dudek, P., Keller, A., Lameyre, J., Le Bas, J., Sabine, M.J., Zanettin, A.R., 1989. A classification of igneous rocks and glossary of terms: recommendations of the International Union of Geological Sciences. Subcommission on the Systematics of Igneous Rocks. 552, 3.
Lentz, D.R., 1998. Petrogenetic evolution of felsic volcanic sequences associated with Phanerozoic volcanic-hosted massive sulphide systems: the role of extensional geodynamics. Ore Geol. Rev. 12 (5), 289–327.
Li, S., Wilde, S.A., Wang, T., 2013. Early Permian post-collisional high-K granitoids from Liuyuan area in southern Beishan orogen, NW China: petrogenesis and tectonic implications. Lithos 179, 99–119.
Liew, T.C., Hofmann, A.W., 1998. Precambrian crustal components, plutonic associations, plate environment of the Hercynian Fold Belt of central Europe: indications from an Nd and Sr isotopic study. Contrib. Mineral. Petrol. 98, 129–138.
Ludwing, K., 2003. User's manual for Isoplot 3.00. A geochronological toolkit for Microsoft Excel. Berkeley Geochronology Center. 4, 1–70.
Ma, X., Cai, K., Zhao, T., Bao, Z., Wang, X., Chen, M., Buslov, M.M., 2018. Devonian volcanic rocks of the southern Chinese Altai, NW China: petrogenesis and implication for a propagating slab-window magmatism induced by ridge subduction during accretionary orogenesis. J. Asian Earth Sci. 160, 78–94.
Mahood, G., Hildreth, W., 1983. Large partition coefficients for trace elements in high-silica rhyolites. Geochim. Cosmochim. Acta 47 (1), 11–30.
McDonough, W.F., Sun, S.S., Ringwood, A.E., Jagoutz, E., Hofmann, A.W., 1992. Potassium, rubidium, and cesium in the Earth and Moon and the evolution of the mantle of the Earth. Geochim. Cosmochim. Acta 56, 1001–1012.
Middlemost, E.A., 1994. Naming materials in the magma/igneous rock system. Earth Sci. Rev. 37, 215–224.
Miller, C.F., McDowell, S.M., Mapes, R.W., 2003. Hot and cold granites? Implications of zircon saturation temperatures and preservation of inheritance. Geology. 31 (6), 529–532.

Morata, D., Aguirre, L., Oyarzun, M., Vergara, M., 2000. Crustal contribution in the genesis of the bimodal Triassic volcanism from the Coastal Range, central Chile. Revista geológica de Chile 27 (1), 83–98.
Mossakovsky, A.A., Ruzhentsev, S.V., Samygin, S.G., Kheraskova, T.N., 1993. Central Asian fold belt: geodynamic evolution and history of formation. Russ. Geotektonika 6, 3–33.
Murzin, O.V., Gorshechnikov, V.I., Chekalin, V.M., Gusev, N.I., Bedarev, N.P., 2001. Geological Report to State Geological Map of the Russian Federation. Altai Series. Scale 1: 200,000. Sheet M-44-X and XI. Second ed. Sankt-Peterburgskaya Kartograficheskaya Fabrika, St. Petersburg, p. 304 (in Russian).
Orihashi, Y., Hirata, T., 2003. Rapid quantitative analysis of Y and REE abundances in XRF glass bead for selected GSJ reference rock standards using Nd-YAG 266 nm UV laser ablation ICP-MS. Geochem. J. 37, 401–412.
Orozco-Esquivel, M.T., Nieto-Samaniego, A.F., Alaniz-Alvarez, S.A., 2002. Origin of rhyolitic lavas in the Mesa Central, Mexico, by crustal melting related to extension. J. Volcanol. Geotherm. Res. 118 (1–2), 37–56.
Patiño Douce, A.E., 1997. Generation of metaluminous A-type granites by low-pressure melting of calc-alkaline granitoids. Geology 25, 743–746.
Patiño Douce, A.E., Beard, J.S., 1996. Effects of P, f(O2) and Mg/Fe ratio on dehydration melting of model metagreywackes. J. Petrol. 37, 999–1024.
Pearce, J.A., Norry, M.J., 1979. Petrogenetic implications of Ti, Zr, Y, and Nb variations in volcanic rocks. Contrib. Mineral. Petrol. 69 (1), 33–47.
Pearce, J.A., Harris, N.B., Tindle, A.G., 1984. Trace element discrimination diagrams for the tectonic interpretation of granitic rocks. J. Petrol. 25, 956–983.
Peccerillo, A., Taylor, S.R., 1976. Geochemistry of Eocene calc-alkaline volcanic rocks from the Kastamonu area, northern Turkey. Contrib. Mineral. Petrol. 58 (1), 63–81.
Piercey, S.J., Nelson, J.L., Colpron, M., Dusel-Bacon, C., Simard, R.L., Roots, C.F., 2006. Paleozoic magmatism and crustal recycling along the ancient Pacific margin of North America, northern Cordillera. Paleozoic evolution and metallogeny of pericratonic terranes at the ancient Pacific margin of North America, Canadian and Alaskan Cordillera. Geol. Assoc. Can. Spec. Pap. 45, 281–322.
Piercey, S.J., Peter, J.M., Mortensen, J.K., Paradis, S., Murphy, D.C., Tucker, T.L., 2008. Petrology and U-Pb geochronology of footwall porphyritic rhyolites from the Wolverine volcanogenic massive sulfide deposit, Yukon, Canada: implications for the genesis of massive sulfide deposits in continental margin environments. Econ. Geol. 103 (1), 5–33.
Pirajno, F., 2010. Intracontinental strike-slip faults, associated magmatism, mineral systems and mantle dynamics: examples from NW China and Altai-Sayan (Siberia). J. Geodyn. 50 (3–4), 325–346.
Polat, A., Hofmann, A.W., 2003. Alteration and geochemical patterns in the 3.7–3.8 Ga Isua greenstone belt, West Greenland. Precambrian Res. 126 (3–4), 197–218.
Promyslova, M.Y., 2004. New concept of the geodynamic nature of the Devonian ore-bearing basalt-rhyolite formation in Rudnyi Altai. Dokl. Earth Sci. 399 (9), 1209–1211.
Rickwood, P.C., 1989. Boundary lines within petrologic diagrams which use oxides of major and minor elements. Lithos 22, 247–263.
Rosenbursh, H., 1923. Elemente der gesteinslehre. Vierte neu bearbeitete Auflage, Stuttgart.
Rotarash, A.I., Samygin, S.G., Gredyushko, Y.A., Keyl'man, G.A., Mileyev, V.S., Perfil'yev, A.S., 1982. The Devonian active continental margin in the southwest Altai. Geotectonics 16.
Rudnick, R.L., Gao, S., 2003. Composition of the continental crust. The Crust. 3. Elsevier, pp. 1–64.
Rutter, M.J., Wyllie, P.J., 1988. Melting of vapour-absent tonalite at 10 kbar to simulate dehydration–melting in the deep crust. Nature 331 (6152), 159.
Safonova, I.Y., Seltmann, R., Kroner, A., Gladkochub, D., Schulmann, K., Xiao, W., Kim, T., Komiya, T., Sun, M., 2011. A new concept of continental construction in the Central Asian Orogenic Belt (compared to actualistic examples from the Western Pacific). Episodes 34, 186–194.
Safonova, I., Maruyama, S., Kruk, N., Obut, O., Kotler, P., Gavryushkina, O., Khromykh, S.V., Kuibida, M., Krivonogov, S., 2018. Pacific-type orogenic belts: linking evolution of oceans, active margins and intra-plate magmatism. Episodes 41, 78–87.
Sajona, F.G., Maury, R.C., Pubellier, M., Leterrier, J., Bellon, H., Cotten, J., 2000. Magmatic source enrichment by slab-derived melts in a young post-collision setting, central Mindanao (Philippines). Lithos 54 (3–4), 173–206.
Sakata, S., Hirakawa, S., Iwano, H., Danhara, T., Guillong, M., Hirata, T., 2017. A new approach for constraining the manitude of initial disequilibrium in Quaternary zircons by coupled uranium and thorium decay series dating. Quat. Geochronol. 38, 1–12.
Samuel, M.D., Moussa, H.E., Azer, M.K., 2007. A-type volcanics in central eastern Sinai, Egypt. J. Afr. Earth Sci. 47 (4–5), 203–226.
Saraev, S.V., Baturina, T.P., Bakharev, N.K., Izokh, N.G., Sennikov, N.V., 2012. Middle–Late Devonian island-arc volcanosedimentary complexes in northwestern Rudny Altai. Russ. Geol. Geophys. 53 (10), 982–996.
Scaillet, B., Holtz, F., Pichavant, M., 2016. Experimental constraints on the formation of silicic magmas. Elements 12 (2), 109–114.
Scherba, G.N., D'yachkov, B.A., Stuchevsky, N.I., Nakhtigal, G.P., Antonenko, A.N., Lubetsky, V.N., 1998. The Great Altai (Geology and Metallogeny). Book 1. Almaty in Russian, Gylym.
Sengör, A.M.C., Natal'in, B.A., Burtman, V.S., 1993. Evolution of the Altaid tectonic collage and Paleozoic crustal growth in Eurasia. Nature 364, 299–307.
Şengör, A.C., Natal'in, B.A., Sunal, G., van der Voo, R., 2018. The tectonics of the Altaids: crustal growth during the construction of the continental lithosphere of Central Asia between ~750 and ~130 Ma ago. Annual Review of Earth and Planetary Sciences 46, 439–494.
Shand, S.J., 1943. Eruptive Rocks: Their Genesis, Composition, and Classification, With a Chapter on Meteorites. Wiley Sons, New York.
Shen, X., Zhang, H., Wang, Q., Wyman, D.A., Yang, Y., 2011. Late Devonian–Early Permian A-type granites in the southern Altay Range, Northwest China: petrogenesis and implications for tectonic setting of "A2-type" granites. J. Asian Earth Sci. 42 (5), 986–1007.
Shinjo, R., Kato, Y., 2000. Geochemical constraints on the origin of bimodal magmatism at the Okinawa Trough, an incipient back-arc basin. Lithos 54 (3–4), 117–137.
Shokalsky, S.P., Babin, G.A., Vladimirov, A.G., Borisov, S.M., Gusev, N.I., Tokarev, V.N., Kruk, N.N., 2000. Correlation of Igneous and Metamorphic Complexes in the Western Altai-Sayan Folded Area. Izd. SO RAN, Novosibirsk. p. 185.
Skjerlie, K.P., Johnston, A.D., 1993. Fluid-absent melting behavior of an F-rich tonalitic gneiss at mid-crustal pressures: implications for the generation of anorogenic granites. J. Petrol. 34, 785–815.
Slama, J., Kosler, J., Condon, D.J., Crowley, J.L., Gerdes, A., Hanchar, J.M., Horstwood, M.S.A., Morris, G.A., Nasdala, L., Norberg, N., Schaltegger, U., Schoene, N., Tubrett, M.N., Whitehouse, M.J., 2008. Plesovice zircon - a new natural reference material for U-Pb and Hf isotopic microanalysis. Chem. Geol. 249 (1–2), 1–35.
Stern, R.A., 1997. Geological survey of Canada current research. Radiogenic Age and Isotopic Studies Report. 10, 1–32.
Sun, S., McDonough, W.F., 1989. Chemical and isotopic systematics of oceanic basalts: implications for mantle composition and processes. In: Saunders, A.D., Norry, M.J. (Eds.), Magmatism in the Ocean Basins, Journal of the Geological, Society, London. 42, pp. 313–345 Special Publication.
Sylvester, P.J., 1989. Post-collisional alkaline granites. J. Geol. 97, 261–280.
Tamura, Y., Gill, J.B., Tollstrup, D., Kawabata, H., Shukuno, H., Chang, Q., Ishizuka, O., 2009. Silicic magmas in the Izu–Bonin oceanic arc and implications for crustal evolution. J. Petrol. 50 (4), 685–723.
Vielzeuf, D., Clemens, J.D., Pin, C., Moinet, E., 1990. Granites, granulites, and crustal differentiation. Granulites and Crustal Evolution. Springer, Dordrecht, pp. 59–85.
Vladimirov, A.G., Kruk, N.N., Rudnev, S.N., Khromykh, S.V., 2003. Geodynamics and granitoid magmatism of collision orogens. Russ. Geol. Geophys. 44, 1321–1338.
Wan, B., Zhang, L., Xiang, P., 2010. The Ashele VMS-type Cu-Zn deposit in Xinjiang, NW China formed in a rifted arc setting. Resour. Geol. 60 (2), 150–164.
Wang, Q., Wyman, D.A., Xu, J., Jian, P., Zhao, Z., Li, C., He, B., 2007. Early Cretaceous adakitic granites in the northern Dabie Complex, Central China: implications for partial melting and delamination of thickened lower crust. Geochim. Cosmochim. Acta 71 (10), 2609–2636.
Watkins, J.M., Clemens, J.D., Treloar, P.J., 2007. Archaean TTGs as sources of younger granitic magmas: melting of sodic metatonalites at 0.6-1.2 GPa. Contrib. Mineral. Petrol. 154 (1), 91–110.
Watson, E.B., Harrison, T.M., 1983. Zircon saturation revisited: temperature and composition effects in a variety of crustal magma types. Earth Planet. Sci. Lett. 64 (2), 295–304.
Watt, G.R., Harley, S.L., 1993. Accessory phase controls on the geochemistry of crustal melts and restites produced during water-undersaturated partial melting. Contrib. Mineral. Petrol. 114 (4), 550–566.
Whalen, J.B., Hildebrand, R.S., 2019. Trace element discrimination of arc, slab failure, and A-type granitic rocks. Lithos 348, 105179.
Whalen, J.B., Currie, K.L., Chappell, B.W., 1987. A-type granites: geochemical characteristics, discrimination and petrogenesis. Contrib. Mineral. Petrol. 95, 407–419.
Whalen, J.B., Jenner, G.A., Longstaffe, F.J., Robert, F., Gariépy, C., 1996. Geochemical and isotopic (O, Nd, Pb and Sr) constraints on A-type granite petrogenesis based on the Topsails igneous suite, Newfoundland Appalachians. J. Petrol. 37 (6), 1463–1489.
White, A.J.R., Chappell, B.W., 1983. Granitoid types and their distribution in the Lachlan Fold Belt, southeastern Australia. Geological Society of America Memoir 159 (12), 21–34.
Wiedenbeck, M., Hanchar, J.M., Peck, W.H., Sylvester, P., Valley, J., Whitehouse, M., Franchi, I., 2004. Further characterisation of the 91500 zircon crystal. Geostand. Geoanal. Res. 28 (1), 9–39.
Wilke, M., Schmidt, C., Dubrail, J., Appel, K., Borchert, M., Kvashnina, K., Manning, C.E., 2012. Zircon solubility and zirconium complexation in $H_2O+Na_2O+SiO_2\pm Al_2O_3$ fluids at high pressure and temperature. Earth Planet. Sci. Lett. 349, 15–25.
Wilson, C.J.N., Blake, S., Charlier, B.L.A., Sutton, A.N., 2005. The 26.5 ka Oruanui eruption, Taupo volcano, New Zealand: development, characteristics and evacuation of a large rhyolitic magma body. J. Petrol. 47 (1), 35–69.
Winchester, J.A., Floyd, P.A., 1977. Geochemical discrimination of different magma series and their differentiation products using immobile elements. Chem. Geol. 20, 325–343.
Windley, B.F., Alexeiev, D., Xiao, W., Kroner, A., Badarch, G., 2007. Tectonic models for accretion of the Central Asian Orogenic Belt. Journal of the Geological Society. London. 164, 31–47.
Wu, Y., Yang, F., Liu, F., Geng, X., Li, Q., Zheng, J., 2015. Petrogenesis and tectonic settings of volcanic rocks of the Ashele Cu–Zn deposit in southern Altay, Xinjiang, Northwest China: insights from zircon U-Pb geochronology, geochemistry and Sr-Nd isotopes. J. Asian Earth Sci. 112, 60–73.
Wu, F., Liu, X., Ji, W., Wang, J., Yang, L., 2017. Highly fractionated granites: recognition and research. Science China Earth Sciences 60 (7), 1201–1219.
Xia, X.P., Sun, M., Zhao, G.C., Li, H.M., Zhou, M.F., 2004. Spot zircon U-Pb isotope analysis by ICP-MS coupled with a frequency quintupled (213 nm) Nd-YAG laser system. Geochem. J. 38, 191–200.
Xiao, L., Clemens, J.D., 2007. Origin of potassic (C-type) adakite magmas: experimental and field constraints. Lithos 95, 399–414.
Xiao, W., Santosh, M., 2014. The western Central Asian Orogenic Belt: a window to accretionary orogenesis and continental growth. Gondwana Res. 25, 1429–1444.
Xiao, W., Huang, B., Han, C., Sun, S., Li, J., 2010. A review of the western part of the Altaids: a key to understanding the architecture of accretionary orogens. Gondwana Res. 18 (2–3), 253–273.
Xu, J.F., Castillo, P.R., Chen, F.R., Niu, H.C., Yu, X.Y., Zhen, Z.P., 2003. Geochemistry of late Paleozoic mafic igneous rocks from the Kuerti area, Xinjiang, northwest China: implications for backarc mantle evolution. Chem. Geol. 193 (1–2), 137–154.

Xu, W.L., Wang, Q.H., Wang, D.Y., Guo, J.H., Pei, F.P., 2006. Mesozoic adakitic rocks from the Xuzhou-Suzhou Area, Eastern China: evidence for partial melting of delaminated lower continental crust. J. Asian Earth Sci. 27 (4), 454–464.
Yakubchuk, A.S., 2004. Architecture and mineral deposit settings of the Altaid orogenic collage: a revised model. J. Asian Earth Sci. 23, 761–779.
Yamada, R., Yoshida, T., Kimura, J.I., 2012. Chemical and Isotopic Characteristics of the Kuroko-Forming Volcanism. Res. Geol. 62 (4), 69–383.
Yang, F., Li, Q., Yang, C., Zhang, Z., 2018. A combined fluid inclusion and S–H–O–He–Ar isotope study of the Devonian Ashele VMS-type copper–zinc deposit in the Altay orogenic belt, northwest China. J. Asian Earth Sci. 161, 139–163.
Yarmolyuk, V.V., Kuz'min, M.I., Vorontsov, A.A., 2013. West Pacific-type convergent boundaries and their role in the formation of the Central Asian Fold Belt. Russ. Geol. Geophys. 54 (12), 1427–1441.
Yolkin, E.A., Sennikov, N.V., Buslov, M.M., Yazikov, A.Y., Gratsianova, R.T., Bakharev, N.K., 1994. Paleogeographic reconstruction of the Western Altai-Sayan area in the Ordovician, Silurian, and Devonian and their geodynamic interpretation. Russ. Geol. Geophys. 35 (7–8), 118–144.
Zhang, C., Santosh, M., Liu, L., Luo, Q., Zhang, X., Liu, D., 2018. Early Silurian to Early Carboniferous ridge subduction in NW Junggar: evidence from geochronological, geochemical, and Sr-Nd-Hf isotopic data on alkali granites and adakites. Lithos 300, 314–329.
Zhu, G., Niu, M., Xie, C., Wang, Y., 2010. Sinistral to normal faulting along the Tan-Lu Fault Zone: evidence for geodynamic switching of the East China continental margin. J. Geol. 118 (3), 277–293.
Zonenshain, L.P., Kuzmin, M.I., Natapov, L.M., 1990. Geology of the USSR: plate tectonic synthesis. Am. Geophys. Union. Geodyn. Ser. Monograph 21.